MICROCOPY RESOLUTION TEST CHART
NATIONAL BUREAU OF

MASSACHUSETTS INSTITUTE OF TECHNOLOGY

LINCOLN LABORATORY

DESIGN CONSIDERATIONS FOR THE
INFRARED AIRBORNE RADAR (IRAR) MTI SUBSYSTEM

R. C. HARNEY

Group 53

PROJECT REPORT TST-26

(Tactical Systems and Technology)

21 JULY 1980

LEXINGTON   MASSACHUSETTS

ABSTRACT

A design for a moving target indication (MTI) subsystem for the infrared airborne radar (IRAR) is investigated. A Doppler MTI system incorporating heterodyne detection and a cw CO_2 laser is determined to be the most suitable approach. Numerous analyses of topics including field-of-view coverage, Dopper resolution, signal-to-noise ratio, clutter effects, etc. are presented which serve to define component specifications and processing requirements. The potential architecture of the MTI system is discussed and the impact of developing technologies on system and component design is estimated.

Accession For

NTIS GRA&I ☑
DTIC TAB ☐
Unannounced ☐
Justification

By
Distribution/
Availability Codes

Dist	Avail and/or Special
A	

CONTENTS

LIST OF ILLUSTRATIONS

1. INTRODUCTION

The goal of the infrared airborne radar (IRAR) program[1-3] is to develop a fire control system for tactical aircraft utilized in a close air support role. The concept of the IRAR system calls for a laser moving target indication (MTI) system to detect targets of interest (i.e., moving targets) and provide a location cue to a high-resolution imaging infrared radar. The imager would be used first to positively verify the identity of a suspected target and later to act as a gunsight for the aircraft's ordnance system. In this report we will examine the design criteria for the IRAR laser MTI subsystem and identify areas which require further investigation

MTI systems can be divided into two general classes: delay line cancellation techniques and Doppler techniques. In the first class of techniques a radar return from the scene obtained with one pulse is subtracted from the return obtained from the preceding pulse. As a result stationary targets will be cancelled out and moving targets will be emphasized. This form of MTI is not particularly suitable for our use for two reasons. First, the aircraft's own motion will cause every object in the scene to shift its position making it difficult to detect those objects which are truly moving. Second, delay line techniques require multiple observations of the scene. Tactical aircraft applications may not permit more than one observation of each point in the scene as the aircraft flies along. Consequently, the IRAR system must utilize a Doppler MTI technique. In a Doppler technique the frequency shifts between the transmitted and received signals are analyzed to determine the relative velocities between objects in the scene and the radar. In

1

a fixed-base installation any Doppler-shifted return indicates a moving target. In an airborne application any difference between the Doppler shift due to the relative speed of the aircraft with respect to the ground and the Doppler shift of an object on the ground indicates that the object is moving.

Several microwave radar MTI systems are currently in use on tactical aircraft and could in principle be employed for cuing the IRAR imager. We have opted for a laser radar MTI system because it offers a possibility for sharing optical components with the imager (and thus achieving additional compactness) which a microwave system does not have.

The basic concept of the proposed IRAR MTI subsystem is as follows. A laser beam illuminates a patch on the ground ahead of the aircraft. A combination of the aircraft's forward motion and a rapid side-to-side scanning of the illuminated patch serves to illuminate the entire ground (at least once) within a specified search field-of-view. The laser radiation reflected by the scene is collected by a telescope and imaged onto a detector system (possibly consisting of an array of detectors). The received radiation is frequency analyzed to yield the relative radial velocity between the aircraft and each portion of the scene. Comparison with the aircraft's

2

ground velocity (possibly obtained by the IRAR MTI system itself or possibly provided by another aircraft subsystem) yields those portions of the scene which are moving with respect to the ground. The MTI system then directs the IRAR imager to image the moving areas for possible hostile target identification.

Although it is highly desirable to have the IRAR MTI subsystem share as many components as possible with the IRAR imager subsystem, we will not restrict ourselves by arbitrarily imposing this restraint. We begin the design analysis by comparing the relative merits of various detector systems and laser systems. These comparisons dictate the use of a cw CO_2 laser-heterodyne detector system to perform the MTI function. Next the conditions imposed by the need for efficient heterodyne detection and adequate coverage of the search field-of-view on the size, shape, and structure of the hetero-dyne detector system are investigated. These aspects of the problem dictate that a large one-dimensional array must be employed. Given the general design of an MTI system as determined from the analyses in the preceding sections, the signal-to-noise ratio (SNR) for realistic values of the parameters envisioned in actual use situations is estimated and the beneficial effects of multiple resolution element integration are investigated. This analysis indicates that resolution element integration is required to extend the operational regime of the IRAR system to include moderately bad weather. The effects of clutter are also considered and clutter is found to have a significant effect on the minimum detectable target velocity. Next, the architecture of the Doppler frequency analyzer and resolution element

3

integration systems are discussed. The potential utility of various emerging technologies (acoustooptic, surface acoustic wave (SAW), and charge-coupled device (CCD)) is also considered. Throughout this report the compatibility of the total MTI subsystem resulting from this work with the proposed IRAR imaging subsystem is analyzed. Although the electronic processing portions of each subsystem are *obviously different, it is found that a single optical system (laser, transmit and receive optics, and detector) can be made to suffice for both the imaging and MTI functions.*

2. CHOICE OF LASER AND DETECTOR SYSTEMS

In the Introduction we gave arguments supporting the use of a Doppler MTI technique in the IRAR system. There are two conceptually different approaches to Doppler MTI. In the first approach the laser radiation returning from an element of the scene is frequency-analyzed by a spectrometer, a set of narrow-band filters, or some other optical device. The dispersed optical signal is then converted to a set of electrical signals by direct detectors, a different detector being used for each spectral resolution element of interest. The electrical signals are subsequently analyzed to determine the Doppler shifts in the scene from which the existence or non-existence of moving targets is deduced. In the second approach the returning laser radiation and radiation from a local oscillator laser are simultaneously detected by a single heterodyne detector. The electrical output from the heterodyne detector contains frequency components which are directly related to the Doppler shifts in the scene. By passing the signal through a bank of parallel electrical bandpass filters or through a real-time Fourier transformer a number of electrical signals are obtained which can be processed as in the

4

first approach to determine the Doppler shifts and thereby deduce the existence or non-existence of moving targets.

The IRAR MTI subsystem should be capable of 2 kmph motion discrimination. To accomplish this the Doppler MTI system must have a frequency resolution capability $R' = \nu/\delta\nu$ of at least 5.4×10^8. Here $\delta\nu$ is the minimum resolvable Doppler shift imposed on a transmitted laser beam of frequency ν. Almost all optical frequency-analyzing devices have resolutions which fall well short of this requirement. For example, narrow-bandpass optical filters have $R' \lesssim 10^4$; typical grating spectrographs have $R' \sim 10^5$; and a very good Fabry-Perot interferometer may have a value for R' approaching 10^8 in the visible region. Although one could in principle build an optical system with the required resolution, it would probably be quite large, very complicated, and extremely sensitive to environmental factors (vibration, temperature, etc). Consequently, we must conclude that the first approach is unsuitable for use in the IRAR system. The maximum theoretical resolution of the heterodyne detection approach is limited only by the laser and local oscillator frequency stabilities and the bandwidth of the electrical circuitry. The electrical bandwidths can be made as narrow as one desires and lasers have been built with frequency stabilities $\nu/\delta\nu$ which are orders of magnitude in excess of the required value of 5.4×10^8. Thus there is no fundamental limitation to using the heterodyne approach in the IRAR MTI subsystem.

The signal-to-noise ratio obtained from a heterodyne detector when shot noise from the local oscillator is the dominant noise source is given by the relation

$$SNR = \frac{\eta P_R}{h\nu B} \qquad (1)$$

5

where η is the heterodyne efficiency, P_R is the signal power incident upon the detector, $h\nu$ is the energy of a signal photon with frequency ν, and B is the larger of the bandwidth of the electrical circuit and the laser bandwidth. Clearly, the transmitter laser should possess the highest possible power and the narrowest possible bandwidth. This double constraint immediately eliminates many of the possible candidate laser systems. Prominent among the remaining candidates are visible noble gas ion lasers, Nd^{3+}:YAG and related solid state lasers, HF or DF lasers, CO lasers, and CO_2 lasers.

The visible noble gas ion lasers are very inefficient, requiring kilowatts of input power to produce a few watts of laser output. For this reason they are unsuitable for airborne applications where the available electrical power is quite limited. Nd^{3+} lasers can be quite efficient when pumped by semiconductor diode lasers. However, a number of factors related to their short wavelength mediate against their use. First, since $h\nu$ appears in the denominator of Eq. (1), the shorter the laser wavelength used the higher the received power must be to yield the same SNR (all other factors being equal). Second, efficient heterodyne detection (maximum η) requires that the signal and local oscillator wavefronts maintain a phase relationship which is constant to within a small fraction of a wavelength over the entire detector area. Examination of Fig. 1 indicates that the maximum phase mismatch between the wavefronts of two collimated beams with angular separation γ incident on a detector of linear dimension ℓ will be

$$\Delta\phi = \frac{x}{\lambda} 2\pi \quad \sim \quad \frac{\gamma\ell}{\lambda} 2\pi \tag{2}$$

6
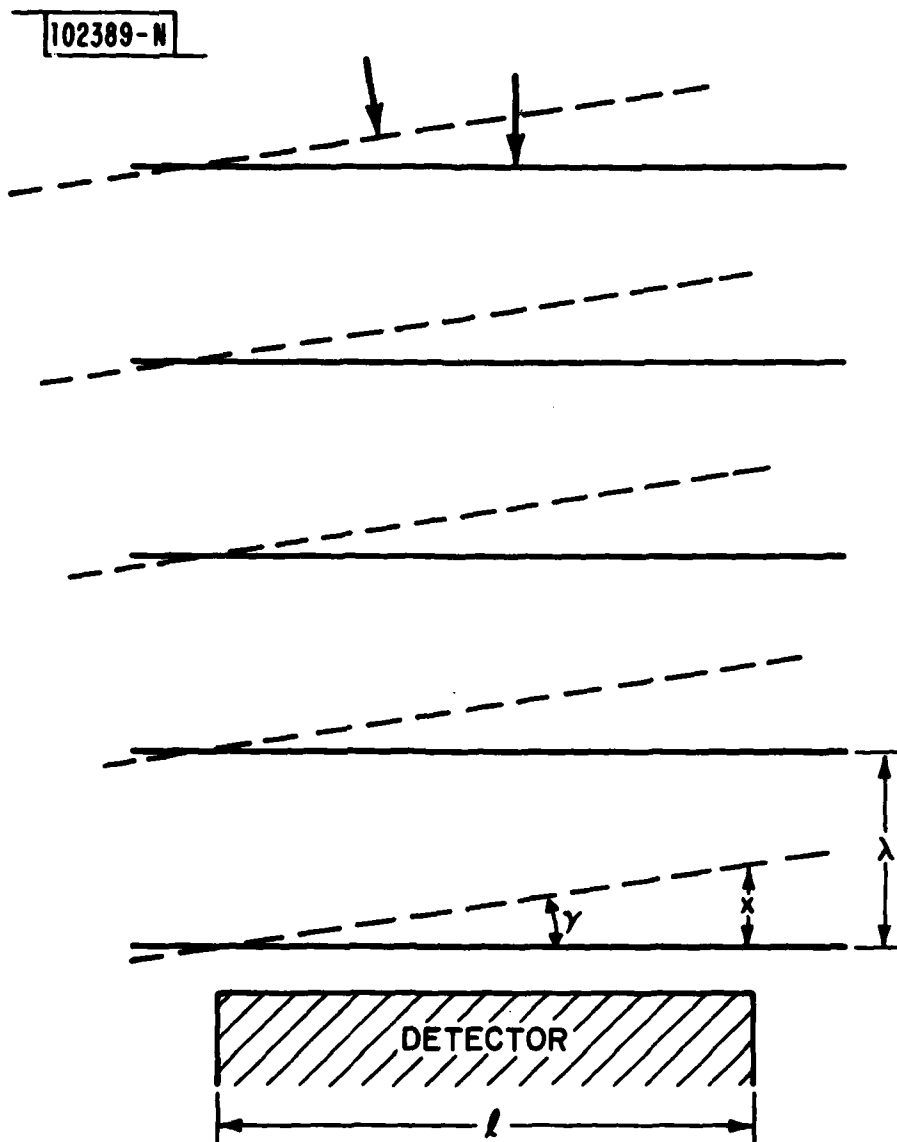
Fig. 1.   Effects of angular mismatch between two collimated wavefronts.

Since efficient heterodyne detection requires $\Delta\phi \ll \pi$, the shorter the incident wavelength the smaller the maximum angular separation that can be tolerated. Third, the absolute frequency stability of a laser becomes harder to control as the wavelength is decreased. This is complicated by the large gain bandwidths of Nd^{3+} lasers which further increases the difficulty of stable operation. Any increase in the bandwidth B results in a decrease in SNR. For these reasons heterodyne detection of Nd^{3+} and other visible and near infrared lasers is a lab curiosity. Longer wavelength lasers are better when heterodyne detection is employed in a field environment.

Atmospheric attenuation is another factor working against short wavelength lasers. Fig. 2 shows atmospheric attenuation data obtained for four laser wavelengths (CO_2 - 10.6 μm, CO - 4.73 μm, DF - 3.83 μm, and Nd^{+3} :YAG - 1.06 μm) in the vicinity of Essen, Germany.[4] In winter, the attenuation at 10.6 μm exceeds 2 dB/km only 15% of the time while the attenuation at 1.06 μm exceeds 2 dB/km 40% of the time. In summer, the attenuation at 10.6 μm exceeds 2 dB/km only 8% of the time while the attenuation at 1.06 μm exceeds 2 dB/km 18% of the time. Attenuation at wavelengths below 1.06 μm is characteristically higher still. Although attenuation data obtained at other sites is quantitatively different, qualitatively the attenuation is always much less at 10.6 μm (and less still at 3.83 μm or 4.73 μm) than at 1.06 μm. Because a small increase in attenuation drastically reduces the received power when detection ranges of several kilometers or more are involved, and in view of the arguments presented in the preceding paragraph, we conclude that Nd^{3+} lasers are unsuitable for use in the IRAR system.

ESSEN, GERMANY
DAYTIME HOURS - 600 TO 1800 LST
FROM 1949 1 1 TO 1952 6 2

ATMOSPHERIC ATTENUATION:
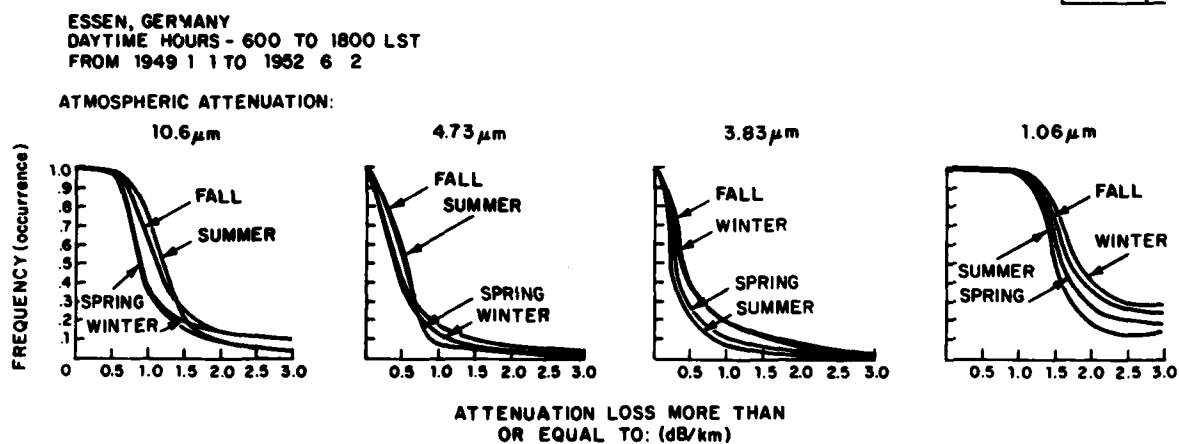
Fig. 2. Seasonal atmospheric attenuation effects in Essen, Germany at four laser wavelengths: CO_2 - 10.6 μm, CO - 4.73 μm, DF - 3.83 μm, and Nd^{3+}:YAG - 1.06 μm. The curves plot the probability that the attenuation is greater than or equal to the value given on the abscissa.

9

Atmospheric attenuation arguments favor using CO or DF lasers over CO_2 lasers. Furthermore, for constant transmitter aperture diameter, the angular resolution of the radar increases with decreasing wavelength. This also favors CO or DF lasers. However, CO lasers operate on a partial population inversion (an inversion between specific rotational levels of different vibrational states without an inversion of the total population of the two vibrational states; this requires a rotational temperature which is significantly lower than the vibrational temperature). As a consequence, efficient operation of CO lasers requires cooling to liquid nitrogen temperatures. This must be done directly in a conventional electric discharge CO laser and would be prohibitive in an airborne application. Cooling is achieved by gas-dynamic processes in a closed-cycle GDL CO laser. However, gasdynamic lasers tend to be quite large and are probably unsuitable for use on a tactical aircraft. High-power DF lasers are typically combustion driven systems requiring high gas flow and an efficient means to exhaust the DF waste product. Such open-cycle systems are impractical for use on tactical aircraft. Closed-cycle electrically-pumped DF lasers operate very similarly to CO lasers and thus would suffer many of the same problems. Therefore, barring significant technological advances in CO or DF laser operation, the logical choice of laser system for use in the IRAR MTI subsystem is a CO_2 laser.

Longitudinal electric discharge CO_2 lasers have long been proven capable of achieving high powers (in either cw or repetitively-pulsed modes), narrow linewidths, and efficient heterodyne detection. Furthermore, they can be made sufficiently compact and efficient to be readily adaptable to airborne

10

use.[5] In an MTI application the question immediately arises as to whether cw or repetitively-pulsed operation is optimum. At CO_2 laser frequencies ($\sim 3 \times 10^{13}$ Hz) the Doppler shift corresponding to 2 kmph target motion is only 106 kHz. To be able to achieve this frequency resolution the effective laser bandwidth must be less than 106 kHz and consequently the laser radiation must have a duration which is in excess of 12 μsec. For a cw laser the effective duration is given by the single pixel dwell time. As will be shown later this can be in excess of 100 μsec. For dwell times in excess of the minimum allowable duration, repetitively-pulsed operation can, in principle, result in increased peak powers with consequent increased signal-to-noise ratios without having the pulse bandwidth exceed the desired Doppler resolution. However, in practice, it is exceedingly difficult to construct compact, efficient, high duty cycle, repetitively-pulsed CO_2 lasers with the desired bandwidth and pulse repetition frequency (PRF) characteristics. Furthermore, as will also be shown later, much of the increase in SNR resulting from pulsed operation can also be realized by suitable post-detection integration of the cw laser signal. Thus, a cw CO_2 laser is the optimum choice for use in the IRAR MTI subsystem.

The choice of appropriate detector material is fairly straightforward. When high frequency heterodyne detection is involved, photovoltaic semiconductor detectors are far superior to photoconductive detectors. Furthermore, detector cooling requirements should be kept to a minimum. At 10.6 μm the only materials available as photovoltaic detectors which can be operated at temperatures as high as 77°K (liquid nitrogen) are $Hg_{(1-x)}Cd_xTe$ and

$Pb_{(1-x)}Sn_xTe$. These two materials have very similar properties, both can be fabricated into arrays, and both make excellent heterodyne detectors at 10.6 μm with high quantum efficiencies. Either would be suitable for use in the IRAR MTI subsystem.

3. SIZE AND SHAPE OF THE HETERODYNE DETECTOR ARRAY

Individual HgCdTe detectors can be made quite small and can be readily incorporated into large one- and two-dimensional detector arrays. A number of factors influence whether a single detector will suffice for use in the IRAR MTI subsystem or whether a detector array is needed. If an array is required, still other factors will determine the optimum number of detectors and the geometry of their arrangement in an array. In this section we will examine the requirements imposed on the detector system by the IRAR MTI mission.

Consider the system shown in Fig. 3. The linear size of a laser beam of wavelength λ transmitted by an aperture of diameter D_T onto a target at range R (assuming diffraction-limited divergence only) is given by

$$L_T \approx R\alpha_T \approx R\lambda/D_T \tag{3}$$

α_T denotes the angular resolution of the transmitter aperture. Approximately equal signs are used in Eq. (3) and succeeding equations because the exact numerical coefficients (all of order unity) depend on the exact intensity profiles of the transmitted beams. The phase correlation distance, L_C, observed at a distant receiver, of the radiation scattered from a diffusely reflecting surface is related to the size of the illuminated region by[6]

102391-N
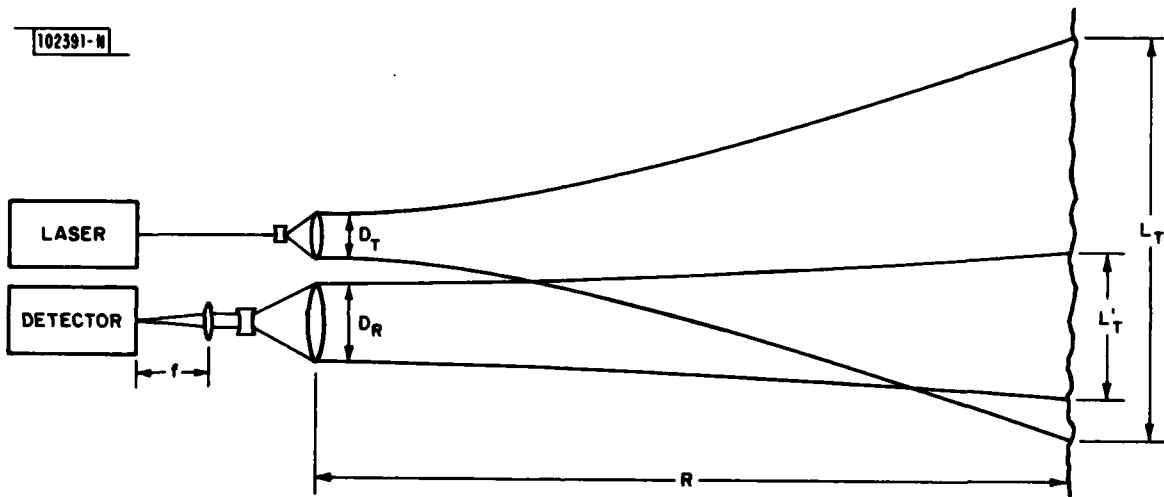
Fig. 3. Receiver and transmitter aperture size effects in an optical radar.

$$L_c \approx \lambda R/L_T \approx D_T \qquad (4)$$

If the receiver aperture (of diameter D_R) is larger than L_c, the lack of phase correlation across the receiver aperture prohibits efficient heterodyne detection with a single detector of all of the radiation scattered from the spot of size L_T.

Consider next a small portion of the illuminated spot. The phase correlation distance at the receiver corresponding to a portion of diameter L_T' is

$$L_c' \approx \lambda R/L_T' \qquad (5)$$

Thus a single detector matched to a receiver of diameter $D_R \approx L_c'$ can efficiently heterodyne the radiation from a portion of the scene of size L_T'. The angular separation of adjacent portions in the scene of size L_T' is given by

$$\alpha_R \approx L_T'/R \approx \lambda/D_R \qquad (6)$$

or just the angular resolution of an aperture of diameter D_R. Thus, if we consider a receiver of diameter D_R and place an array of closely-spaced detectors at the focal plane of a lens imaging the receiver aperture such that each detector looks at a different portion of the illuminated scene of size L_T', an efficient heterodyne output can be obtained from each. The number of detectors required to completely cover the illuminated scene is given roughly by the ratio of the illuminated area to the area viewed by a

14

single detector, i.e.,

$$N \approx \left(\frac{L_T}{L_T'}\right)^2 = \left(\frac{D_R}{D_T}\right)^2 \qquad (7)$$

If it is desired to obtain a single value from the whole illuminated spot, the outputs of the N detectors must be incoherently added. Coherent addition of the outputs is not viable because the heterodyne signals retain information on the optical phase. The lack of phase correlation across the aperture that prevents efficient heterodyne detection with a single detector results in a lack of phase correlation between the N detectors which prevents coherent addition of the outputs.

The preceding results were derived for target plane spot sizes produced solely by diffraction from the apertures. However, they are equally valid for spot sizes produced by artificially diverging (with a negative lens) the beam coming from a larger aperture. As the aperture diameters are no longer the factors determining the divergences, the forms of the preceding expressions which involve the spot sizes (L_T, L_T') and beam divergences (α_T, α_R) alone should be employed for calculational purposes.

Now let us consider an aircraft in level flight with velocity V and altitude H projecting a laser beam onto the ground at slant range R (see Fig. 4). Let the transmitter have an aperture of diameter D_T and the transmitted beam have (lens-induced) divergences $\alpha_x = N_x \alpha_T$ and $\alpha_y = N_y \alpha_T$ where $\alpha_T = \lambda/D_T$, N_x and N_y are constants (≥ 1), x is the direction perpendicular to the plane defined by the altitude and slant range vectors, and y is the direction

102392-N
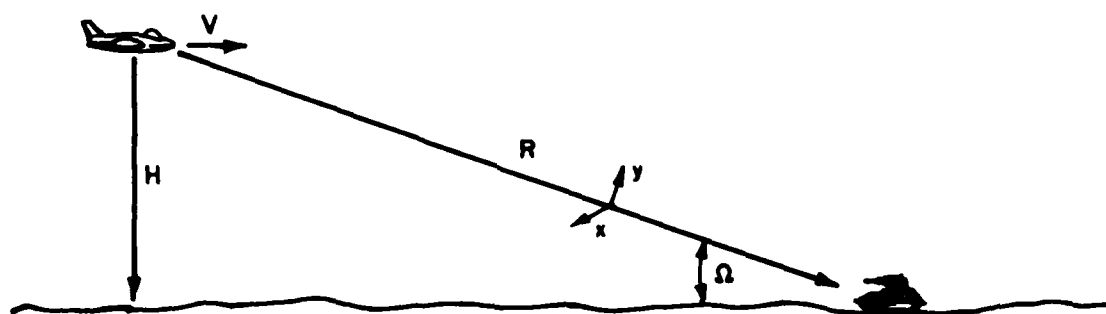
Fig. 4. Geometry encountered in the tactical aircraft application of the IRAR system.

perpendicular to both the x-direction and the slant range vector. The physical size of the beam when projected onto the ground is

$$L_x = 2\alpha_x R = 2N_x \alpha_T R \tag{8}$$

for the x-direction and

$$L_y = 2\alpha_y R/\sin\Omega = 2N_y \alpha_T R(R/H) \tag{9}$$

for the y-direction.

The time required for the aircraft to move forward a distance equal to L_y is

$$t_y = L_y/v = 2N_y \alpha_T R^2/HV \tag{10}$$

If we assume that the beam is swept along the ground in the x-direction by a scanner, the time required to complete a scan with a field-of-view θ_x is

$$t_x = \theta_x/\beta\dot{\omega} \tag{11}$$

where $\dot{\omega}$ is the angular scan rate and β is the retrace efficiency (scan time divided by scan time plus retrace time). In a search mode it is desirable to illuminate every portion of the ground (within the x-direction field-of-view) at least once. This is accomplished when $t_y \geq t_s$, that is, when

$$\dot{\omega} \geq \theta_x HV/2\beta N_y \alpha_T R^2 \tag{12}$$

Typical scanners are limited to modest scan rates, thus for some values of the parameters θ_x, β, H, V, α_T, R, and $\dot{\omega}$ it may be necessary to have $N_y \gg 1$ in order to satisfy Eq. (12).

17

Assume that the illuminated spot is viewed by a receiver with aperture D_R. A detector array consisting of $n_x \times n_y$ detectors, where n_x and n_y are the minimum-valued integers such that

$$n_x \geq N_x D_R/D_T \tag{13}$$

and

$$n_y \geq N_y D_R/D_T, \tag{14}$$

is required to efficiently heterodyne detect the radiation scattered by the spot. If all other parameters are held constant the signal-to-noise ratio of the output of each detector is inversely proportional to the number of detectors

$$SNR = \beta'/n_x n_y \tag{15}$$

because each detector looks at only a fraction of the illuminated spot and thereby receives only the laser radiation scattered from that fraction. β' contains the dependences on laser power, optical efficiency, collection solid angle, atmospheric attenuation, and target reflectivity.

Targets of interest typically encompass a number of receiver resolution elements or pixels. To allow maximum operational utility of the system in bad weather, the system must have the highest possible SNR. Incoherent integration (addition) of the outputs from a number of pixels (all of which lie on the target) yields an improvement in the SNR. Specifically, incoherent integration of the outputs of n'_x detectors along the scan direction in

each row of the array yields an improvement G_x [7]

$$1 \leq G_x < n'_x \qquad (n_x \geq n'_x \geq 1) \tag{16}$$

while incoherent integration of the outputs of n'_y detectors in each column of the array yields an improvement G_y

$$1 \leq G_y < n'_y \qquad (n_y \geq n'_y \geq 1) \tag{17}$$

Furthermore, each detector looks at any given pixel for one dwell time

$$t_D = \lambda/D_R\dot{\omega} \tag{18}$$

but is on an object n'_x pixels wide for n'_x dwell times. Consequently, temporal integration of the signal from each detector over n'_x dwell times gives a SNR improvement G_t

$$1 \leq G_t < n'_x \tag{19}$$

Thus the final SNR which can be obtained for a two-dimensional array with an effective resolution of $n'_x \times n'_y$ pixels is

$$SNR_{2D} = \beta' G_x G_y G_t/n_x n_y \tag{20}$$

In the special case of a one-dimensional array ($n_x = 1$), no spatial integration can be performed in the x-direction and $G_x = 1$. As with the two-dimensional array spatial integration in the y-direction yields a gain given by Eq. (17) while temporal integration yields a gain given by Eq. (19).

Thus, assuming that the transmitted beam is shaped to match a one-dimensional array according to Eqs. (13) and (14), the final SNR which can be obtained for a one-dimensional array with an effective resolution of $n'_x \times n'_y$ pixels is

$$SNR_{1D} = \beta' G_y G_t / n_y = (n_x / G_x) \, SNR_{2D} \tag{21}$$

Since from Eq.(16) $G_x < n'_x \le n_x$, we find that $SNR_{1D} > SNR_{2D}$. Each detector in the array must have its own Doppler analyzer. Therefore, the two-dimensional array requires n_x times as many analyzers as the one-dimensional array. As a result we find that a one-dimensional array is superior to a two-dimensional array in a line scan MTI application for reasons of both system simplicity and increased signal-to-noise ratio.

Efficient heterodyne detection with a one-dimensional array requires that the spot size viewed by the receiver aperture be larger than the transverse size of the illuminated spot. Thus we find that we must have

$$N_x D_R / D_T \le 1 \tag{22}$$

Since the signal received by a detector increases as the square of the receiver diameter, it is clear that we want to make D_R as large as possible. This coupled with the fact that $N_x \ge 1$ implies that the optimum situation arises when

$$D_R = D_T \quad \text{and} \quad N_x = 1$$

i.e., when there is no lens-induced divergence in the x-direction and the receiver and transmitter apertures are of equal size. Given this situation

20

both system simplicity and system compactness then dictate that the transmitter and receiver should share the same aperture.

The same arguments that favor a one-dimensional array over a two-dimensional array, also favor a single detector over a one-dimensional array. However, as shown earlier, complete coverage of the scene may require $N_y \gg 1$. If $N_y \gg 1$ and $D_R = D_T$, then a single detector is insufficient and a one-dimensional array must be used.

The complete expression governing the signal-to-noise ratio obtained for any individual detector in a one-dimensional array is [1]

$$SNR = \frac{P_t}{N_D h \nu B} \frac{D_R^2}{4R^2} \epsilon \rho \eta e^{-2kR} \qquad (23)$$

where P_T is the transmitted laser power, N_D is the total number of detectors in the array, ϵ is the efficiency of the optical system, ρ is the target reflectivity, e^{-2kR} is the round trip atmospheric attenuation, and the remaining parameters have their previously-defined meanings. Because we require complete coverage of the ground within the horizontal field-of-view in the line scan mode of operation, the receiver aperture, the number of detectors, and the required bandwidth are all interdependent. That is, if the minimum number of detectors required to cover the complete scene for a given D_R and $\dot{\omega}$ are used, changing any one of N_D, D_R, $\dot{\omega}$, or B will cause changes in the others. If we separate out all of the interdependent factors, we may write Eq. (23) as

$$SNR = \beta' \frac{D_R^2}{N_D B} \qquad (24)$$

If the system bandwidth is limited by the dwell time of the laser beam on a single pixel, then from Eqs. (12) and (18) we have

$$B = B_D = 1/t_D = \dot{\omega}/2\alpha_R = \dot{\omega}D_R/2\lambda$$

$$= \theta_x HVD_R/2\beta\lambda N_D\alpha R^2 = \theta_x HVD^2_R/2\beta\lambda^2 R^2 N_D \qquad (25)$$

Substituting Eq. (25) into Eq. (24) we find

$$SNR = \beta' \frac{D_R^2}{N_D B_D} = 2\beta'\beta\lambda^2 R^2/\theta_x HV$$

$$= \frac{P_T}{h\nu} \frac{\beta\lambda^2}{2\theta_x HV} \epsilon\rho\eta e^{-2kR} \equiv SNR_o \qquad (26)$$

Thus, the signal-to-noise ratio obtained when the MTI system is dwell time band-width-limited is independent of the receiver aperture or the scan rate. It is determined by the laser power, the mission requirements (H, V, θ_x, R, and k), and the system efficiency. This conclusion does not contradict any of our earlier statements, because earlier we allowed the possibility that $D_R \neq D_T$, a possibility that was subsequently shown to be non-optimum.

If the bandwidth of the system is not dwell time-limited but instead is limited by laser stability (or minimum obtainable Doppler filter bandwidth) then

$$B = B_L$$

In this case Eq. (24) becomes

$$SNR = \beta' \frac{D_R^2}{N_D B_L} = SNR_o(B_D/B_L) \qquad B_D \leq B_L \qquad (27)$$

That is, the signal-to-noise ratio in the laser bandwidth-limited regime is lower than that which would be obtained for a dwell-time bandwidth-limited system with identical D_R and $\dot{\omega}$. The behavior of Eqs. (26) and (27) as a function of B_D/B_L is summarized in Fig. 5. For $B_D \leq B_L$, the SNR is laser bandwidth-limited and Eq. (27) is valid, while for $B_D \geq B_L$ the SNR is dwell bandwidth-limited and obeys Eq. (26). It should be noted that this behavior is characteristic of the optimized MTI line scan mode of operation and would not necessarily be valid for any other mode of IRAR operation.

As mentioned earlier, fluctuations in the effective target reflectivity (due to speckle or atmospheric turbulence) will reduce the MTI detection probability. Thus it is desirable to integrate the returns from a number of pixels (all of which lie on the target) to increase the detection probability. This, of course, requires that

$$2\alpha_T R = 2\lambda R/D_T \ll L \qquad (28)$$

where L is a characteristic target dimension. For targets of 2 m characteristic dimension located at ranges of the order of 3 km, Eq. (28) is satisfied for aperture diameters of the order of 10 cm or larger.

Other factors also affect the choice of aperture size. First, the fact that the entire system must be capable of being carried by a tactical

23
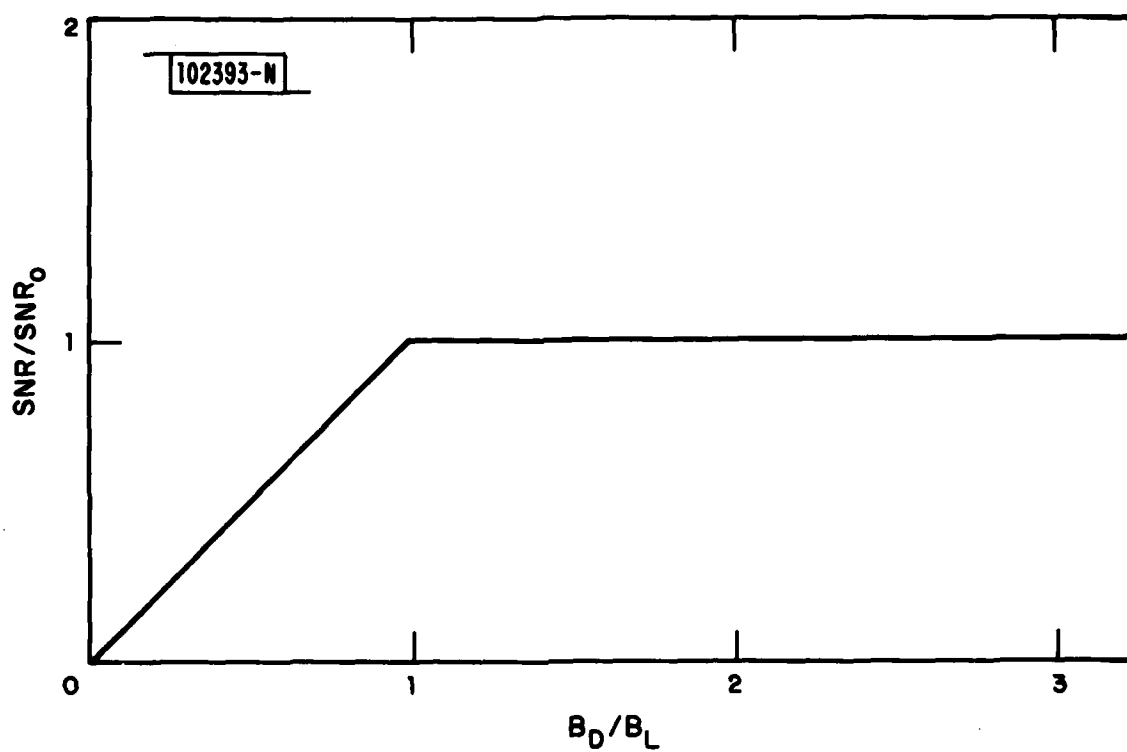
Fig. 5.   Summary of bandwidth effects on the signal-to-noise ratio of an MTI system. B_D is the dwell bandwidth, B_L is the laser bandwidth, and SNR_O is the dwell bandwidth-limited signal-to-noise ratio.

aircraft will in practice limit the maximum aperture that can be used. In
addition, the larger the aperture, the larger the scanner mirror that is
required and the slower the maximum scan rate that can be achieved in practice.
Slower scan rates coupled with smaller resolution angles resulting from
increased aperture sizes mean that more detectors are required for adequate
coverage of the scene. This in turn means an increase in the size and com-
plexity of the MTI electronic processing system. Consideration of all of
the above factors indicate that the aperture of the IRAR MTI system should
fall somewhere in the range of 10-30 cm diameter. Finally, it is highly
desirable that the IRAR MTI subsystem be compatiable with the IRAR imager
subsystem. Since the imager aperture has been sized at approximately 10 cm
for angular resolution reasons, we will henceforth assume this value for the
MTI system as well.

Given all of the preceding information we are now in a position to esti-
mate the size of detector array that is required by the IRAR MTI system.
Maximum scan rates for a 10 cm diameter full aperture scanner are probably
limited to values of the order of 1 rad/sec with 70% retrace efficiency. If
we consider an aircraft flying at 150 m/sec ($\sim$ Mach 0.5) at 50 m altitude
(values compatible with a close air support mission) and searching a 1 radian
field-of-view at 3 km slant range, we find from Eq. (12)

$$N_D \geq 13$$

It is interesting to note that a 13-element one-dimensional array is very
close to the 12-element array proposed for the IRAR imager system. For the

above system parameters, from Eq. (18) we find a dwell time of

$$t_D = 100 \ \mu sec.$$

with a corresponding bandwidth of 10 kHz.

4. SIGNAL-TO-NOISE RATIO AND CLUTTER-TO-NOISE RATIO CONSIDERATIONS

The ability of any MTI system to detect a moving target is profoundly influenced by system noise. Because the optimum technique for detecting the presence of a signal in noise is a simple threshold test, random noise spikes can exceed the threshold level and give false alarms. If the threshold is raised high enough to limit false alarms to an acceptable rate, low-level signals may not be strong enough to exceed the threshold and the detection probability will be reduced. The interrelationships of the detection probability P_D, the false alarm probability P_F, and the signal-to-noise ratio SNR are summarized in receiver operating characteristic (ROC) curves.

For targets obeying speckle statistics (i.e., diffusely reflecting targets), P_D, P_F, and SNR are related by the expression[8]

$$P_D = P_F^{(1 + SNR)^{-1}} \tag{29}$$

ROC curves appropriate to Eq. (29) are plotted in Fig. 6 for several values of P_F.

For an MTI system with N_D detectors and N_C Doppler channels of bandwidth B_C per detector, the false alarm probability required in each channel is

26
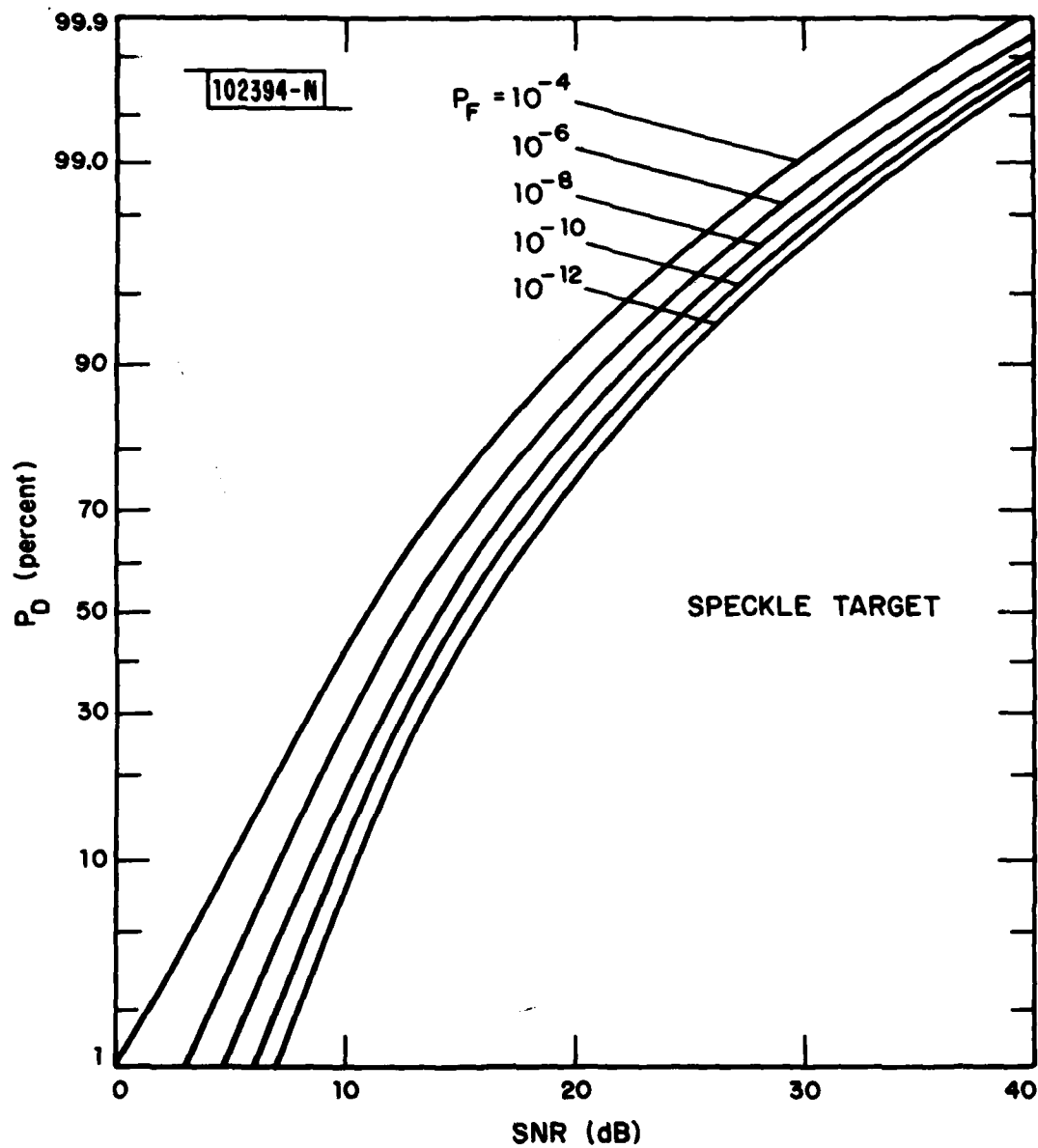
Fig. 6. Receiver operating characteristic curves for speckle targets.

$1/N_D N_C$ times the false alarm probability desired for the system as a whole. Thus,

$$P_F = 1/N_D N_C B_C T_F \qquad (30)$$

where T_F is the required mean time between false alarms for the system as a whole. If the Doppler signal returned from a single pixel has a bandwidth which is less than the Doppler channel bandwidth, then the SNR calculated from Eq. (23) may be compared directly with the abscissa of Fig. 6. This condition should hold for a properly-designed CO_2 laser MTI system. If it is not valid, the result of Eq. (23) must be reduced by the ratio of the bandwidths. This occurs because any one Doppler channel will be capable of passing only a fraction of the total signal.

Typical parameters for the IRAR system are summarized in Table I. Using these values and assuming an average target reflectivity ρ of 0.1 and an atmospheric attenuation of 2 dB/km (this or a lesser value will occur 65% of the time in Central Europe[1,4]), Eq. (23) yields

$$SNR \approx 15.5 = 11.9 \text{ dB}$$

For false alarm times T_F of the order of 15 minutes, we obtain from Eq. (30)

$$P_F \approx 10^{-11}$$

Consulting Fig. 6 we find that the system signal-to-noise ratio is woefully inadequate to achieve detection probabilities greater than 90% with $P_F = 10^{-11}$.

28

TABLE I

TYPICAL PARAMETERS FOR THE IRAR SYSTEM

Laser power - P	10 W cw
Photon energy - $h\nu$	1.87×10^{-20} J
Number of detectors - N_D	12
Number of Doppler channels - N_C	100
Bandwidth per channel - B_C	100 kHz
Dwell bandwidth - B_D	10 kHz
Aperture diameter - D_R	10 cm
Maximum range - R	3 km
Optical efficiency - ϵ	0.1
Heterodyne Efficiency - η	0.5

For speckle targets the receiver operating characteristics at high P_D values are dominated by the probability that speckle will cause a deep fade in the received signal with a resultant failure to exceed the threshold level. If several independent pixels, all of which lie on the target, are examined, the probability that at least one of the returns will exceed the threshold is greatly increased. If N returns are examined, the detection probability becomes

$$P_D(N) = 1 - (1 - P_F^{(1 + SNR)^{-1}})^N \qquad (31)$$

The dashed curve in Fig. 7 shows the number of pixels which must be examined to yield $P_D = 0.99$ and $P_F = 10^{-12}$ as a function of the single-pixel signal-to-noise ratio. For SNR = 11.9 dB, at least 22 pixels must lie on the target. Since a typical tactical target at 3 km range will occupy 50-100 pixels, some degree of multiple-pixel processing is certainly allowable.

However, simply setting the threshold to give the desired single-pixel P_F value and hoping that the number of pixels on the target is large enough so that at least one return exceeds the threshold is by no means optimal. A much more efficient method is to incoherently add the returns from N pixels and compare the integrated signal with a threshold which is a function of the number of pixels integrated. The P_D/P_F effects of pixel integration can be mathematically evaluated using moment generating function techniques.[9] The solid curve in Fig. 7 shows the number of pixels which must be integrated to achieve $P_D = 0.99$ and $P_F = 10^{-12}$ as a function of the single-pixel SNR.[10] For SNR = 12 dB, pixel integration requires only 7 pixels as opposed to 22
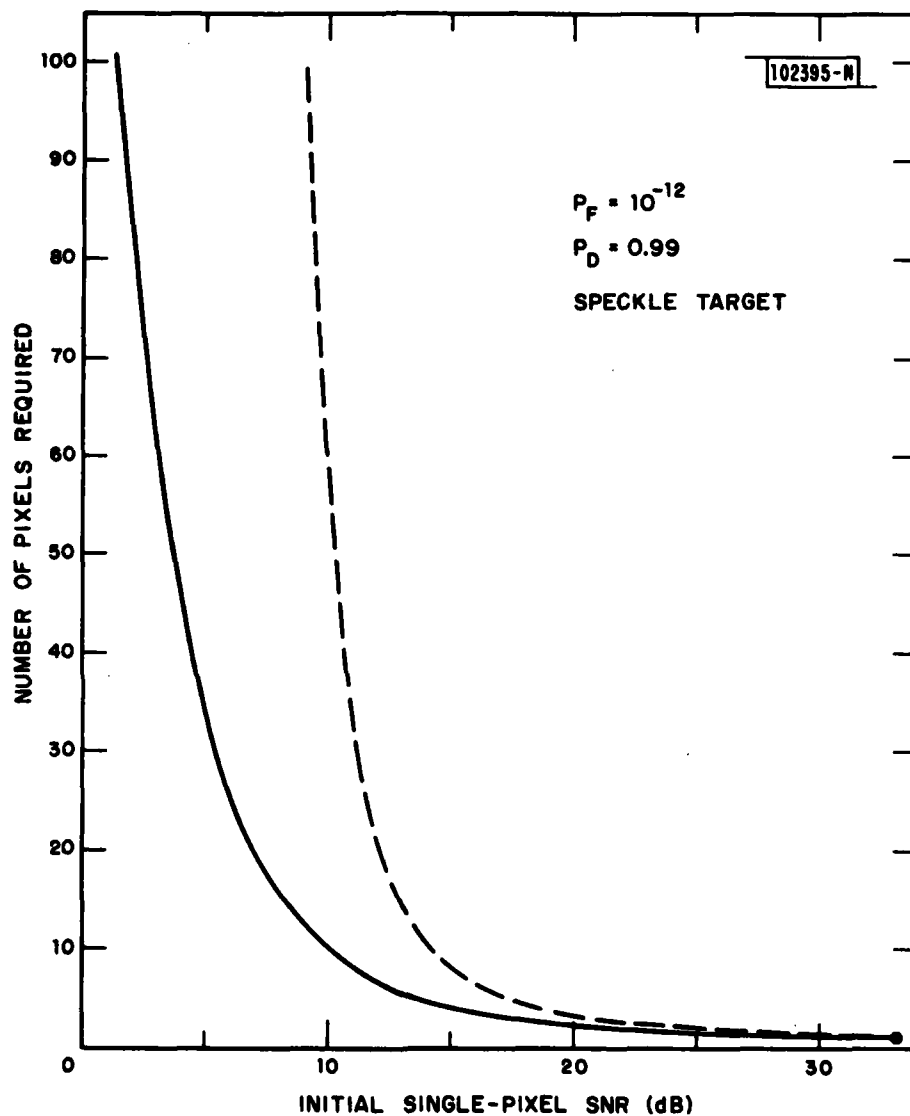
Fig. 7. Speckle target multiple-pixel processing improvement curves for $P_D = 0.99$ and $P_F = 10^{-12}$. The dashed curve gives the number of target returns which must be examined as a function of the single-pixel SNR if the threshold is set to yield the desired P_F on a single-pixel basis and no integration is performed. The solid curve gives the number of pixels which must be integrated if the threshold is set to be optimum for a signal consisting of N incoherently added target returns.

pixels in the single-pixel threshold approach. It should be noted that the curves in Fig. 7 are not strong functions of either P_D or P_F.

The preceding results are valid for speckle (diffusely-reflecting) targets. Some objects, however, exhibit specular reflections called glints. Glints do not fluctuate like speckle targets and therefore will have different P_D/P_F behavior. The detection probability for a glint target is given by[8]

$$P_D = Q_1[(2 \text{ SNR})^{1/2}, (-2 \text{ } \ell n P_F)^{1/2}] \qquad (32)$$

where $Q_1[u, v]$ is Marcum's Q function.[9] ROC curves appropriate to Eq. (32) are plotted in Fig. 8.[11] Comparison of Figs. 6 and 8 indicates that much lower signal-to-noise ratios are required to detect glint targets than to detect speckle targets at high P_D values. This suggests that the presence of target glints may reduce the need for multiple-pixel processing. However, as we shall see, this is only partially true.

If the threshold is chosen to produce the desired single-pixel P_F and N pixels (all containing a glint target) are examined without integration, the effective detection probability is given by

$$P_D(N) = 1 - (1 - Q_1[(2 \text{ SNR})^{1/2}, (-2 \text{ } \ell n P_F)^{1/2}])^N \qquad (33)$$

Eq. (33) has been used to evaluate the number of pixels required to obtain $P_D = 0.99$ with $P_F = 10^{-12}$ for various SNR values. These results are summarized in the dashed curve of Fig. 9. As with speckle targets pixel integration produces much better results for glint targets than does the single-pixel
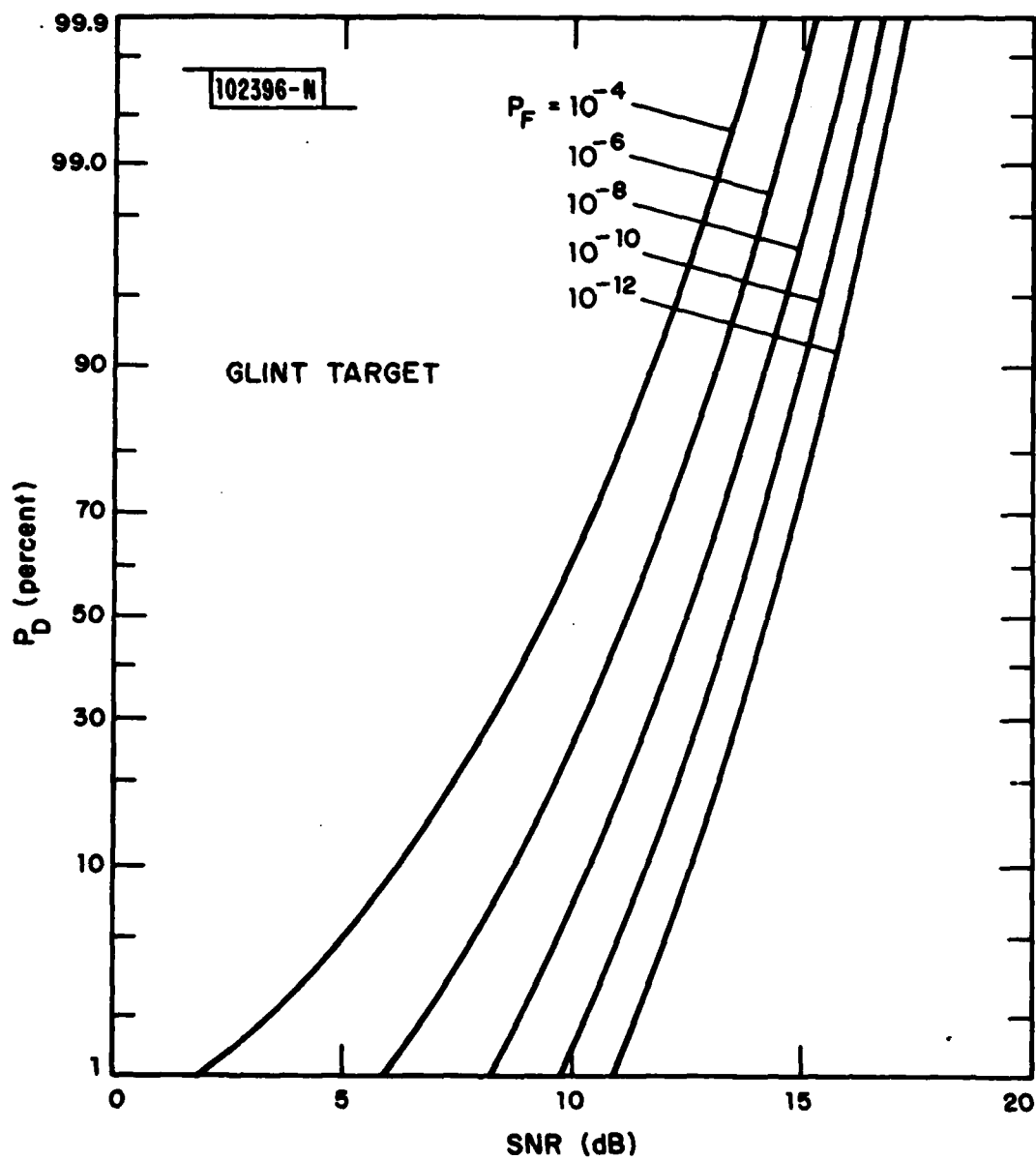
Fig. 8. Receiver operating characteristic curves for glint targets.

33
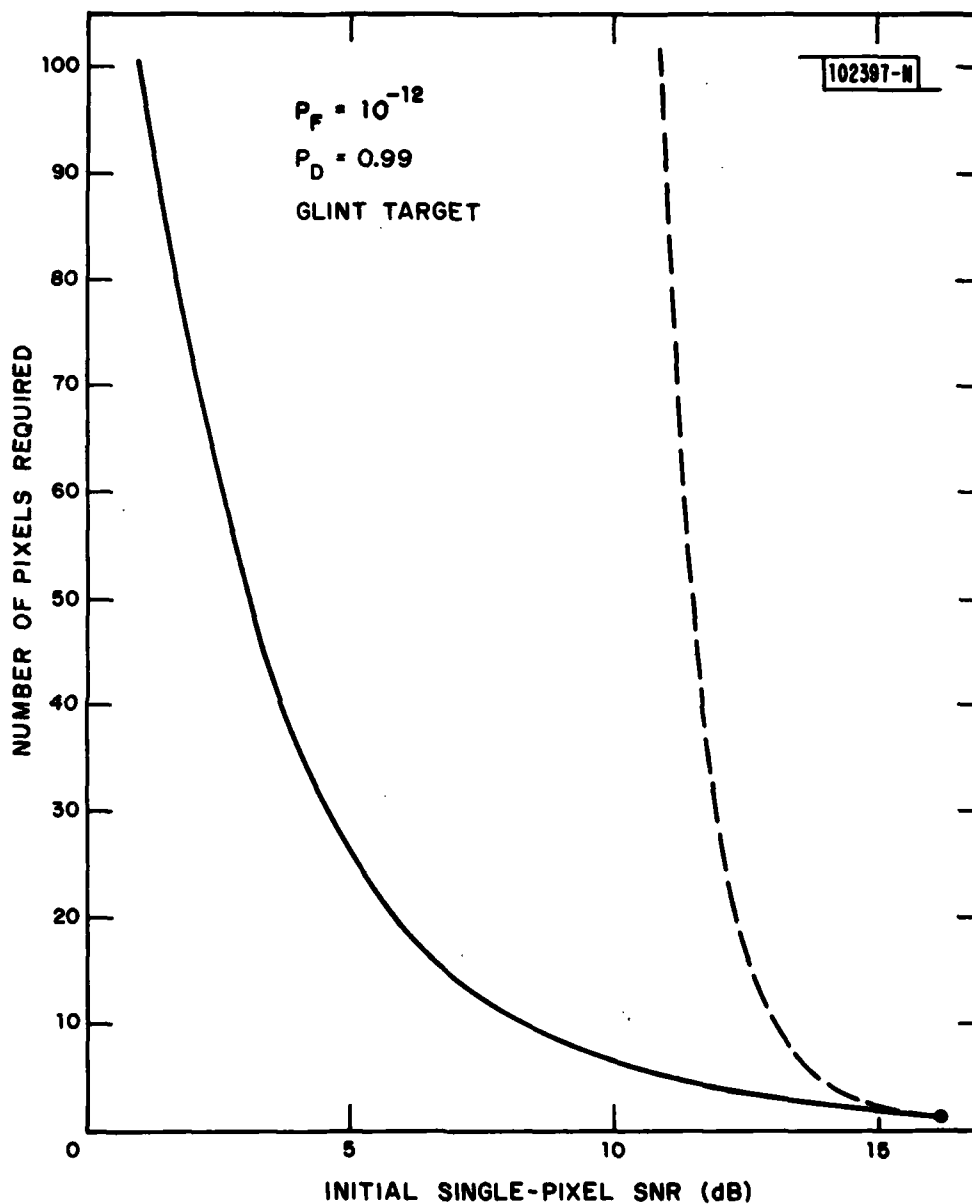
Fig. 9. Glint target multiple-pixel processing improvement curves for P_D = 0.99 and P_F-12. The dashed curve represents results obtained for the single-pixel threshold approach. The solid curve represents results obtained for the pixel integration approach.

34

threshold approach. Using moment generating function techniques the solid curve of Fig. 9 was obtained.[10] Close comparison of Figs. 7 and 9 shows that for glint targets multiple-pixel processing is not required for SNR $\gtrsim$ 16 dB while for speckle targets this condition is only satisfied for SNR $\gtrsim$ 33 dB. However, for SNR $\lesssim$ 10 dB comparable numbers of pixels must be processed for either glint or speckle targets. Thus, if the target glints produce returns which are much stronger than the expected speckle returns ($\sim$ 10-15 dB) pixel integration will not be required, while if the glint returns are only of the same average strength as the expected speckle returns, pixel integration will be a necessity. Since the presence of strong target glints cannot be counted on, some degree of pixel integration must be incorporated into the MTI system.

If the Doppler channel bandwidth B_C is significantly larger than the dwell bandwidth B_D, an additional improvement in signal-to-noise ratio may be realized by performing a postdetection integration operation on each channel before pixel integration. This is possible because, in heterodyne detection, target speckle will cause the signal to vary on time scales of the order of $1/B_D$ while the noise contribution will vary on time scales of the order of $1/B_C$. Thus, in general, n_t independent signal-plus-noise measurements may be made during the time it takes for the laser beam to scan across a single pixel, where

$$n_t = B_C/B_D \tag{34}$$

The improvement in signal-to-noise ratio which may be obtained by integrating n_t measurements after envelope detection of the IF signal is plotted in Fig. 10. This curve is derived from data in Ref. 11 for P_D = 0.99 and P_F = 10^{-12}. Again these results are quite weak functions of P_D and P_F.

Depending on the magnitude of n_t the additional SNR gained by postdetection integration may significantly reduce the number of pixels which must be averaged. In our numerical example of Table I, B_C/B_D = 10, which yields a SNR improvement of approximately 9 dB. This would reduce the speckle averaging requirement from 7 to 2 pixels. Since postdetection integration still does not eliminate the need for pixel integration in most cases, the optimum approach is to use postdetection integration and integration of as many pixels as possible while insuring that the number of pixels integrated is less than the number of pixels on the target. For tactical targets at ranges of interest and allowing for different target orientations, the maximum number of pixels which may be integrated is approximately 25-30. If in the numerical example 30 pixels were integrated instead of 2, an additional 15 dB of SNR margin is obtained. This margin would allow the system to operate out to 3 km even if the atmospheric attenuation were as high as 4.5 dB/km. Thus maximizing the number of pixels integrated maximizes the operational utility of the MTI system.

It should be noted that postdetection integration of $n_t' = n_x' \, n_t$ measurements corresponds to pixel integration of n_x' pixels for each detector of a one-dimensional array, in addition to postdetection integration of n_t
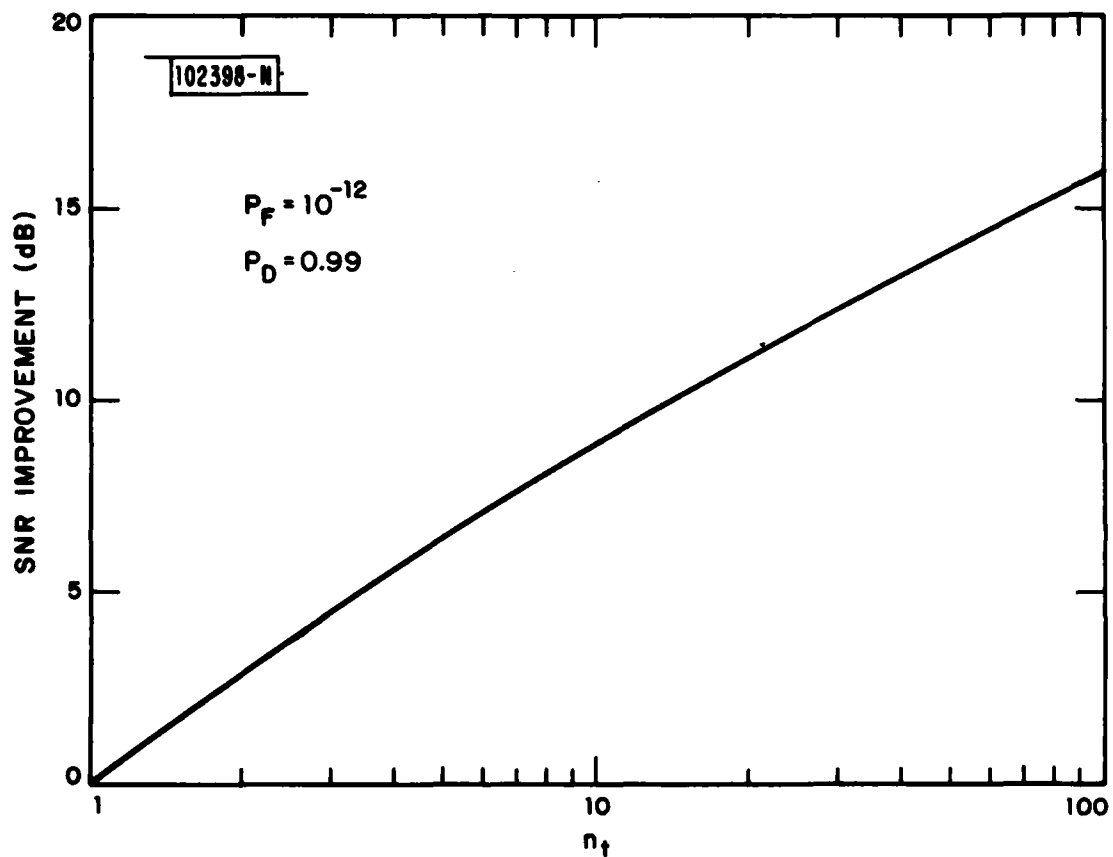
Fig. 10.   Signal-to-noise ratio improvement obtained by postdetection integration of n_t independent signal-plus-noise measurements for $P_D = 0.99$ and $P_F = 10^{-12}$.

measurements. It also corresponds to the temporal integration gain G_t mentioned in the preceding section.

Ground clutter can have a significant effect on the performance of any Doppler MTI system. Windblown trees, shrubbery, and water waves can produce radar returns with non-zero Doppler shifts which might be mistaken for slowly-moving targets. Furthermore, because any filter technique has only a finite rejection for signals outside its bandpass, filter leakthrough of zero velocity signals can affect the effective noise level and thus the effective false alarm probability.

The analysis of clutter effects is generally very complicated. However, by making certain assumptions the problem can be simplified considerably. First, we assume that clutter and target returns are mutually exclusive. That is, the IF signal received from each pixel consists of either clutter-plus-noise or target-plus-noise, but not clutter-plus-target-plus-noise. In a high resolution radar (capable of imaging objects), this is a good approxima-tion. Second, we assume that both the target and the clutter returns obey speckle statistics. This represents a worst (although highly probable) case from the target standpoint, and a typical case from the clutter standpoint. Of all natural clutter sources only water waves are expected to produce moving glint returns.

For a speckle target the detection probability P_{DT} is related to the false alarm probability (caused by noise alone) P_F and the target signal-to-noise ratio SNR by Eq. (29). For radar returns from clutter obeying speckle

statistics and having clutter signal-to-noise ratio CNR, the detection probability P_{DC} is given by

$$P_{DC} = P_F^{(1 + CNR)^{-1}} \tag{35}$$

However, any detected clutter return is essentially a false alarm. Therefore, in a realistic (i.e., cluttered) scenario we may define an effective false alarm probability

$$P'_F = P_{DC} \tag{36}$$

Combining Eqs. (29), (35), and (36) we find for SNR >> 1

$$P'_F = P_{DT}^{(1 + SNR)/(1 + CNR)} \approx P_{DT}^{(\frac{1}{SNR} + \frac{CNR}{SNR})^{-1}} \tag{37}$$

The behavior of P'_F versus the clutter-to-signal ratio CNR/SNR is plotted in Fig. 11 for target detection probability P_{DT} = 0.99 and several values of the noise-only false alarm probability P_F. Fig. 11 indicates that clutter returns must be kept at least 50 dB below the target returns or the effective false alarm probability will be significantly increased above its noise-only value.

The preceding results are valid for single-pixel detection. However, we have already seen that pixel integration is required to solve the target detection problem. Using moment generating function techniques the effect of pixel integration on the P'_F versus CNR/SNR curves can also be evaluated.[10] In Fig. 12 we compare curves for integration of 1, 10, and 50 pixels with P_{DT} = 0.99 and P_F = 10^{-12}. Even with pixel integration clutter must still

39
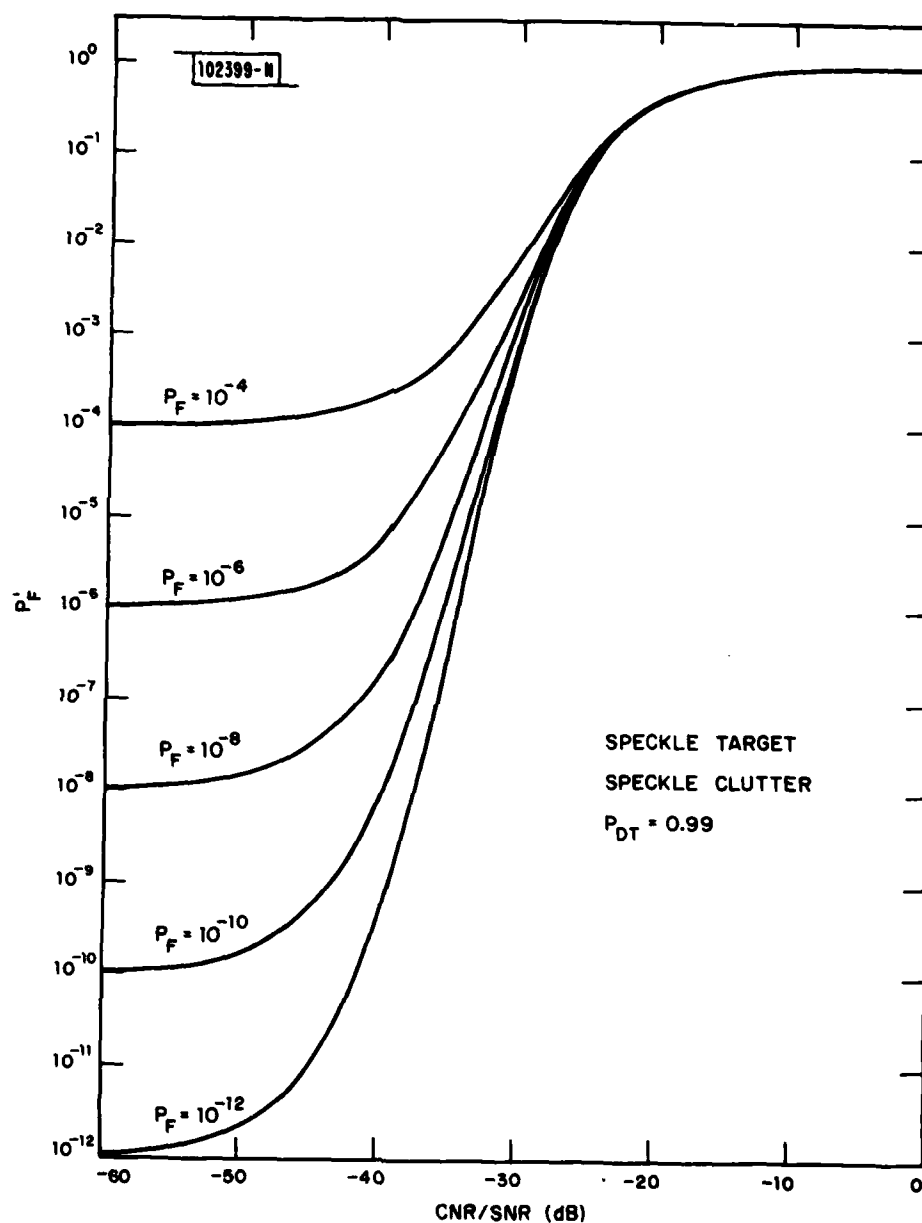
Fig. 11. Effects of varying the clutter-to-signal level on the effective
false alarm probability. Curves are plotted for various noise-only false alarm
probabilities (P_F) and assume speckle targets, speckle clutter, and target
detection probability P_{DT} = 0.99.

40
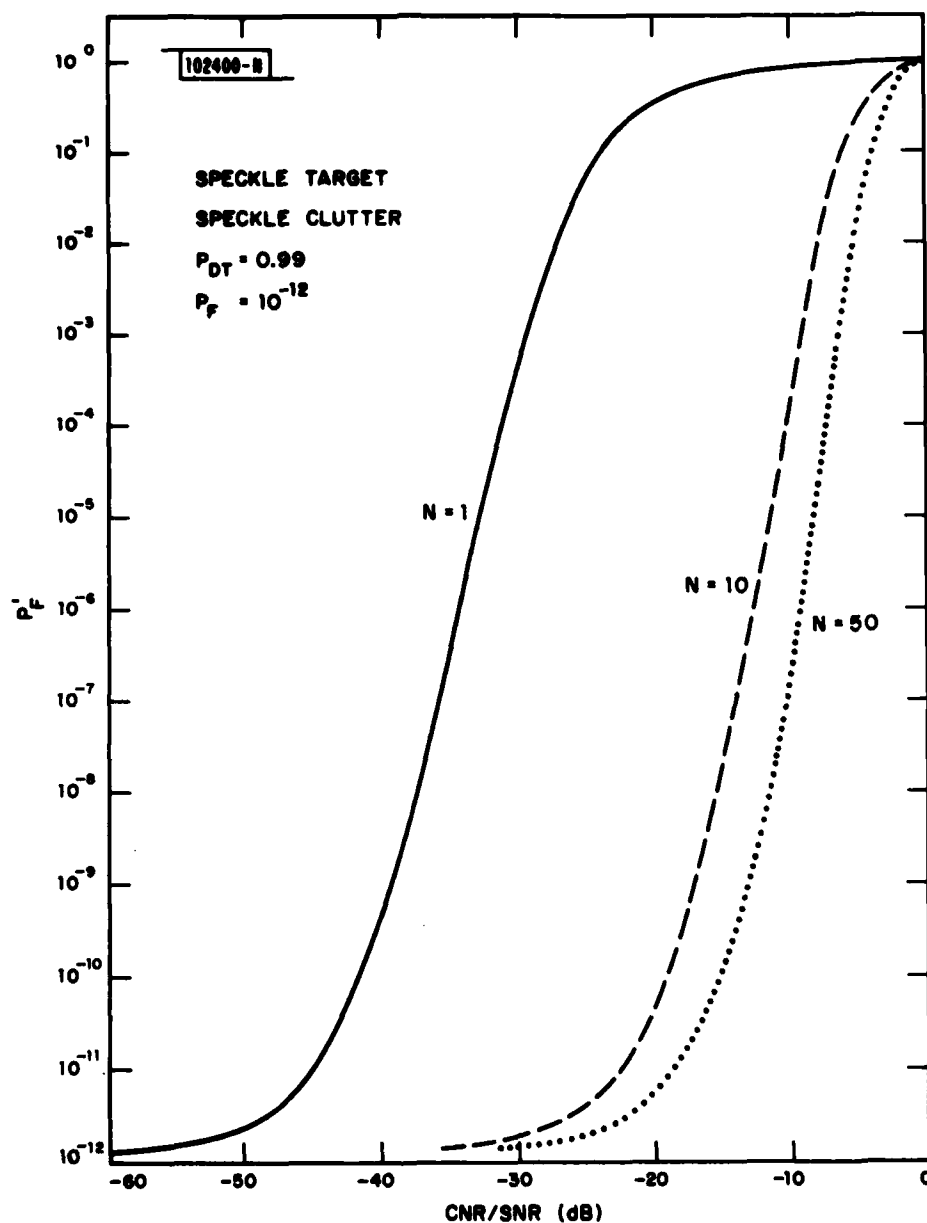
Fig. 12. Effects of pixel integration on the effective false alarm probability versus clutter-to-signal level curves. Curves are plotted for 1, 10, and 50 pixels integrated and assume speckle targets, speckle clutter, $P_F = 10^{-12}$, and $P_{DT} = 0.99$.

41

be kept 25-30 dB below the signal strength or the effective false alarm probability will be significantly increased.

The average clutter return is expected to be of roughly the same strength as the average target return. Thus, low clutter-to-signal ratios can only be achieved if the clutter and target returns are well separated in frequency. Since clutter returns will be distributed in frequency about zero Doppler shift and any realistic filter has some small response out to significant distances from its center frequency, achieving a desirable false alarm probability will impose a nonzero limit on the minimum detectable target velocity.

Measurements of clutter frequency spreads obtained at microwave frequencies indicate that land clutter obeys a Gaussian frequency distribution[12]

$$p(\omega) = (2\pi\sigma^2)^{-1/2} \exp[-\omega^2/2\sigma^2] \tag{38}$$

with standard deviations σ between roughly 0.1 and 1 kmph depending on the wind speed and type of vegetation. Since microwave radars look at large projected areas on the ground, one interpretation of these results is that the individual moving scatterers (leaves, branches, etc.) have velocities which are Gaussianly distributed. If the angular resolution of the radar is poor, many scatterers will be contained in each pixel and each clutter return will have a broadband Gaussian frequency spread. If the angular resolution is very high, only a single moving scatterer will be contained in each pixel and a single-frequency return (neglecting the linewidth of the incident radiation) will result. In this limit Eq. (38) gives the probability of

obtaining a return at any given Doppler shift. The system performance in these two limits will be markedly different.

Let us consider the broadband limit first. An indication of the minimum detectable velocity can be be obtained by considering a frequency analyzer which consists of a bandpass filter whose center frequency can be varied. We assume a filter function of the form

$$f(\omega - \omega_0) = [1 + (\frac{\omega - \omega_0}{\omega_c})^{12}]^{-1} \tag{39}$$

where ω_0 is the center frequency and ω_c is the 3-dB half-bandwidth of the filter. Further clarification of this system can be found in Fig. 13. Eq.(39) approximates the response of a 6-cavity LC filter of bandwidth $2\omega_c$. Given a radar return with a Gaussian spectrum centered at zero frequency, the signal coming out of the filter is proportional to the quantity I

$$I(\omega_0, \omega_c, \sigma) = \int_{-\infty}^{\infty} p(\omega) \, f(\omega - \omega_0) \, d\omega \tag{40}$$

We will now make the assumption that the target has the same frequency spread as the clutter, but is shifted in frequency. Using this assumption, which will be shown shortly to be better than it first appears, the clutter-to-signal ratio may be written as

$$\frac{CNR}{SNR} = \frac{I(\omega_0, \omega_c, \sigma)}{I(0, \omega_c, \sigma)} \tag{41}$$

43
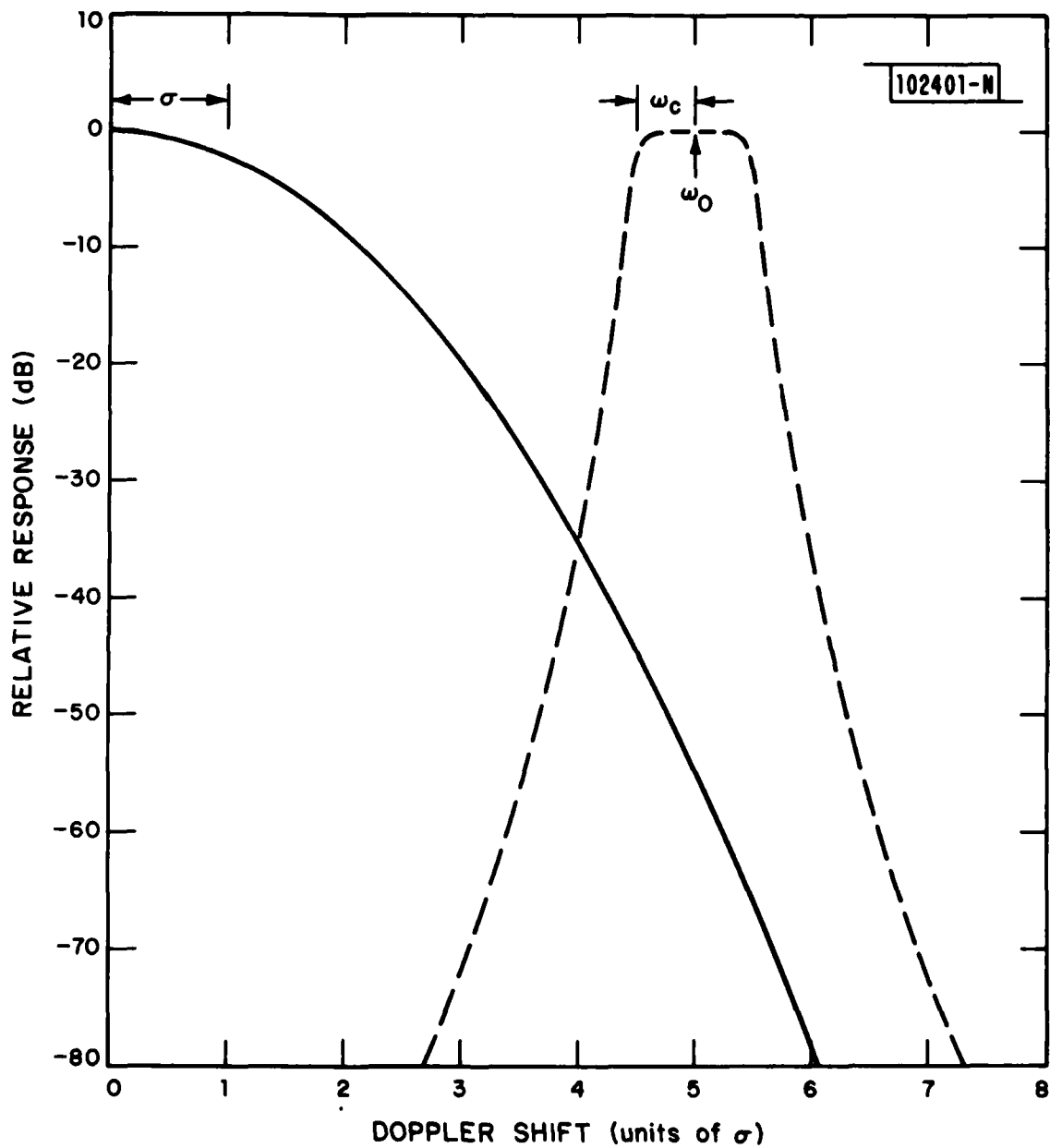
Fig. 13. Functional relationships of MTI clutter model. The solid curve
represents a Gaussian frequency distribution with standard deviation $\sigma = 1.0$.
The dashed curve represents the response of a 6-cavity LC filter of bandwidth
$2\omega_C$ (= 1.0 σ in this example) and center frequency ω_0 (= 5.0 σ).

44

If we identify the Doppler resolution with the quantity $2\omega_c$ and the minimum detectable Doppler shift with the value ω_o such that CNR/SRN = -50 dB (yielding an acceptable false alarm probability), upon evaluation of the convolution integrals (Eq. (40)) we can obtain a family of performance curves parametric in σ. In Fig. 14 the minimum detectable Doppler shift is plotted as a function of the Doppler resolution for σ = 1.0, 1.25, 1.5, and 2.0. These values were chosen because the actual frequency spread of clutter returns is determined by the convolution of the clutter profile with the laser frequency profile (also Gaussian). Since at infrared frequencies σ(laser) $\approx$ 1 kmph and σ(clutter) $\approx$ 0.1 - 1.0 kmph, σ values between 1 and 2 kmph are to be expected. No units are indicated in Fig. 14 because the computations have been carried out for the case of ω_o, ω_c, and σ having the same units, and are therefore valid for any consistent choice of units. Because σ(laser) dominates σ(clutter) in many cases, target and clutter returns will have roughly the same frequency spreads. It should also be noted that the oscillations in the curves are real and not artifacts of the computational procedure.

The effects of integrating returns from 10 pixels have been estimated by performing the same convolutions as before but now identifying the minimum detectable velocity with the value of ω_o such that CNR/SNR = -30 dB. As determined from Fig. 12, CNR/SNR = -30 dB results in an acceptable effective false alarm probability when 10 pixels are integrated. The results of this analysis are given in Fig. 15.

We will now investigate the single-frequency return limit. Referring to Fig. 11 we note that if a return has CNR/SNR $\gtrsim$ -20 dB, it has a high probability of being detected. Therefore, the effective false alarm probability (ignoring

45

102402-N

MINIMUM DETECTABLE VELOCITY

15

$\sigma = 2.0$

10

1.5

1.25

5

1.0

BROADBAND DOPPLER RETURNS
WITH GAUSSIAN FREQUENCY
PROFILE

$P_F' \approx 10^{-12}$, $P_{DT} = 0.99$

0

5

10

DOPPLER RESOLUTION

Fig. 14. Minimum detectable velocity (Doppler shift) versus Doppler resolution as a function of the frequency width of the returns (σ) for the broadband return Gaussian frequency profile limit of clutter behavior. The circles represent numerically - calculated values. $P_F' \approx 10^{-12}$, $P_{DT} = 0.99$.

46
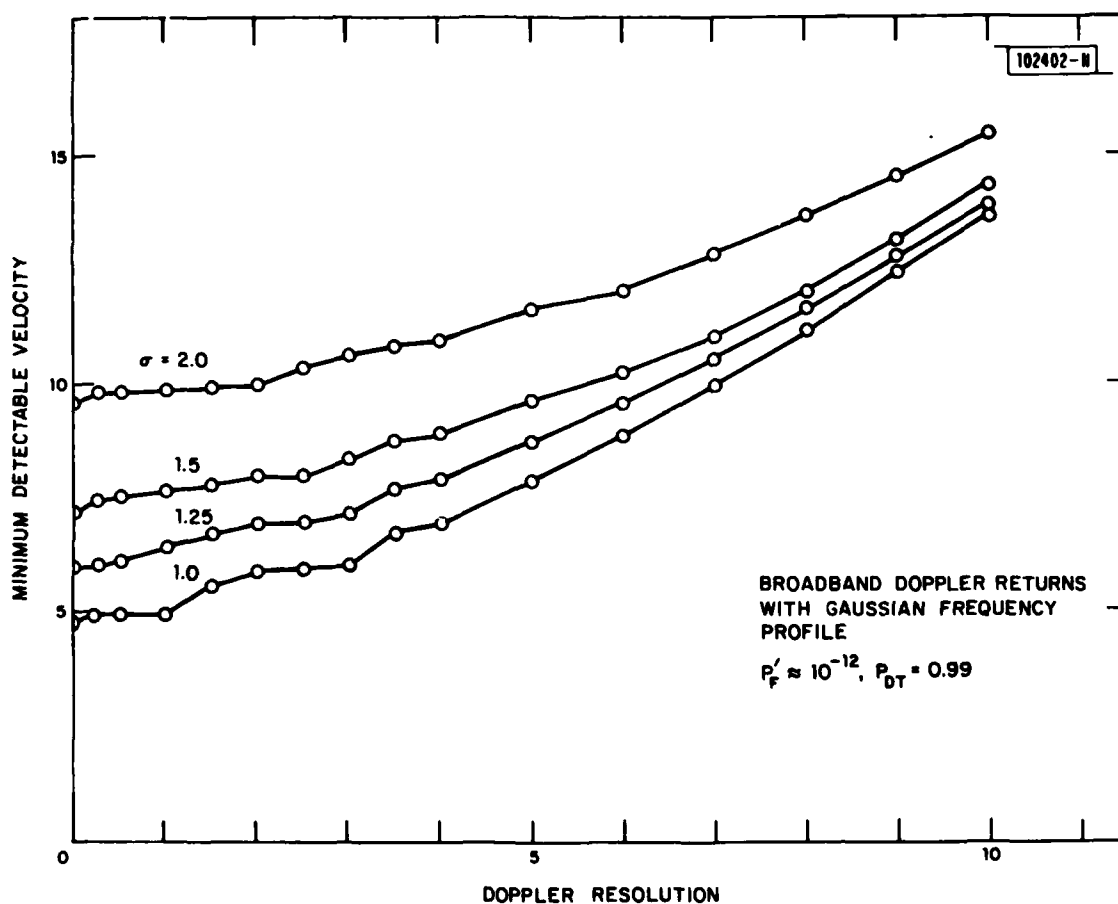
Fig. 15. Minimum detectable velocity (Doppler shift) versus Doppler resolution as a function of the frequency width of the returns (σ) for the broadband return Gaussian frequency profile limit of clutter behavior. Returns from 10 pixels have been integrated to produce these results. The circles represent numerically - calculated values. $P_F' \approx 10^{-12}$, $P_{DT} = 0.99$.

47

noise false alarms) is approximately given by the probability that a single-frequency return occurs within the 20 dB bandwidth of the filter. This probability is given by

$$P'_{DC} (\omega_o, \omega_c, \sigma) \approx \int_{\omega_o - 1.5\omega_c}^{\omega_o + 1.5\omega_c} p(\omega) \, d\omega \qquad (42)$$

Since we assume a unit response when $\omega_o = 0$, we find

$$P'_F \approx P'_{DC} (\omega_o, \omega_c, \sigma)/P'_{DC} (0, \omega_c, \sigma) \qquad (43)$$

Performing these integrations and identifying the minimum detectable velocity with the value of ω_o, such that the desired $P'_F(\approx 10^{-12}$ in this example) is obtained, we obtain curves such as those in Fig. 16.

The effects of integrating 10 pixels have also been investigated in the single-frequency limit. Referring to Fig. 12 we note that the detection probability in the 10-pixel case is roughly unity for CNR/SNR $\gtrsim -5$ dB. Thus, the false alarm probability is approximately given by the probability that a single-frequency return occurs within the 5 dB bandwidth of the filter. This probability is given by Eq. (42) with limits of integration of $\omega_o \pm 1.05\omega_c$. Curves of the minimum detectable velocity as a function of Doppler resolution for $P'_F \approx 10^{-12}$ are shown in Fig. 17.

The preceding clutter results are summarized for $\sigma = 1.0$ in Fig. 18. Examination of these curves indicates several features:

1) There is a substantial difference in minimum detectable velocity
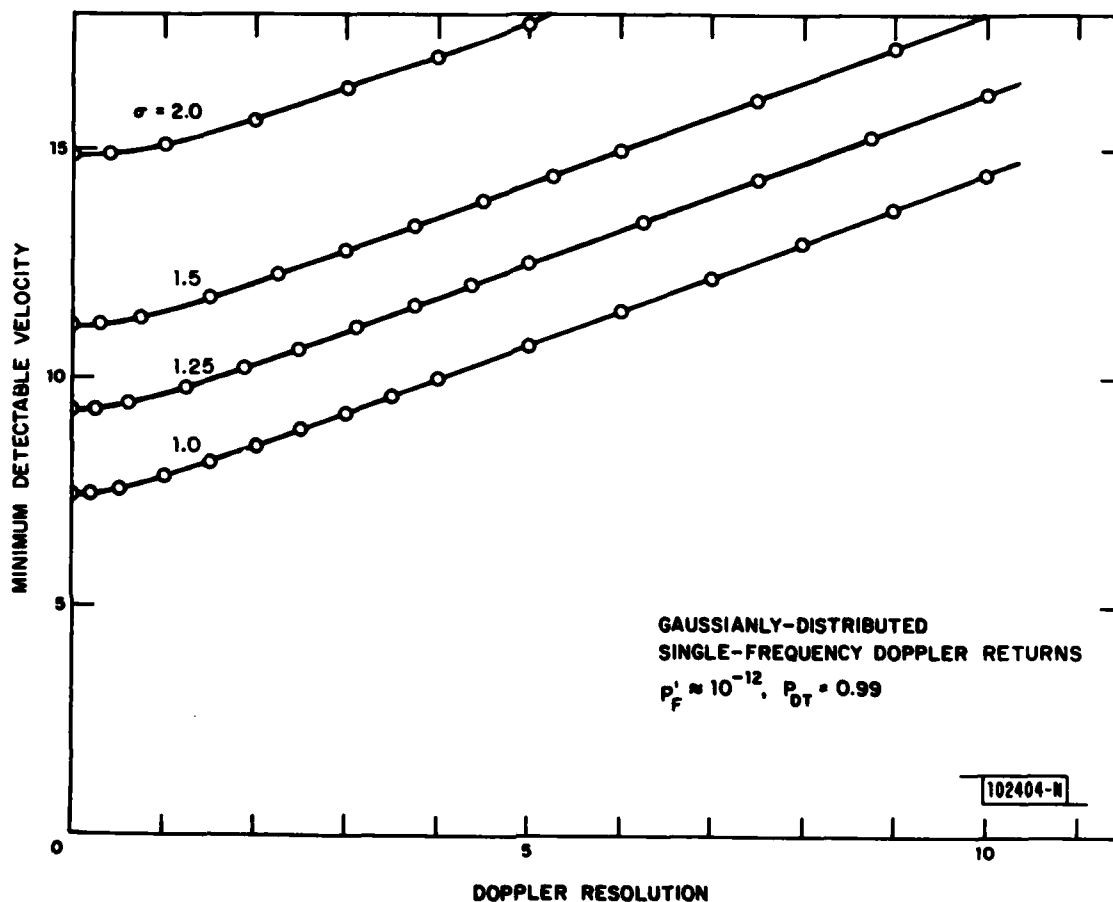
Fig. 16. Minimum detectable velocity (Doppler shift) versus Doppler resolution as a function of the width of the probability distribution (σ) for the single-frequency return Gaussian probability distribution limit of clutter behavior. The circles represent numerically - calculated values. $P_F' \approx 10^{-12}$, $P_{DT} = 0.99$.

49

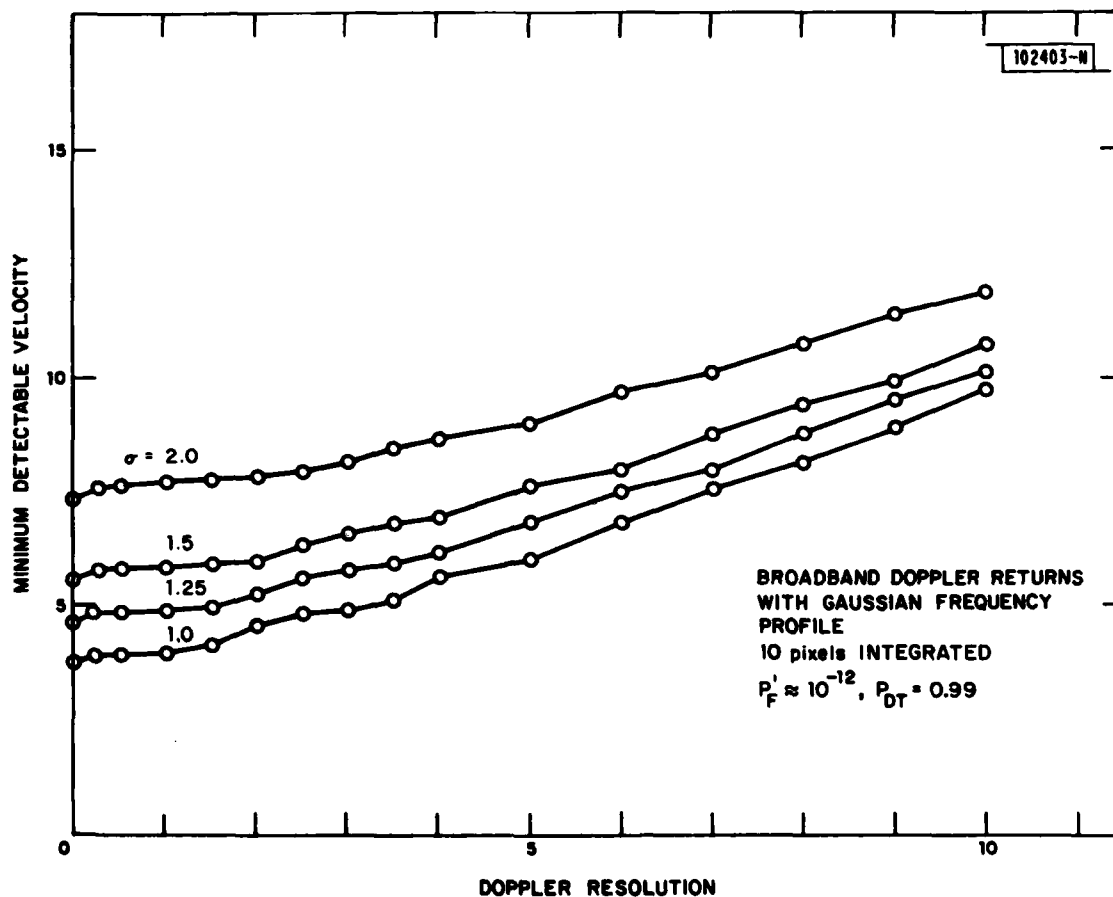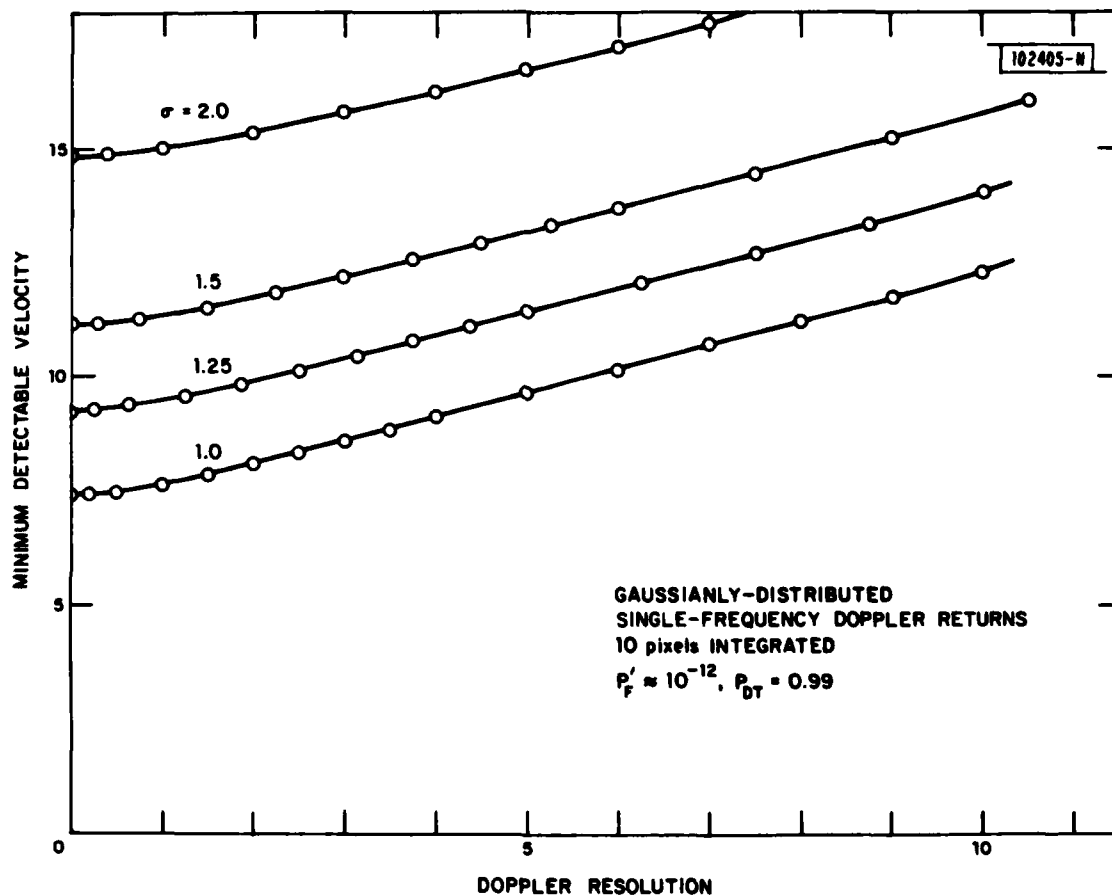Fig. 17. Minimum detectable velocity (Doppler shift) versus Doppler resolution as a function of the width of the probability distribution (σ) for the single-frequency return Gaussian probability distribution limit of clutter behavior. Returns from 10 pixels have been integrated to produce these results. The circles represent numerically - calculated values. $P_F' \approx 10^{-12}$, $P_{DT} = 0.99$.
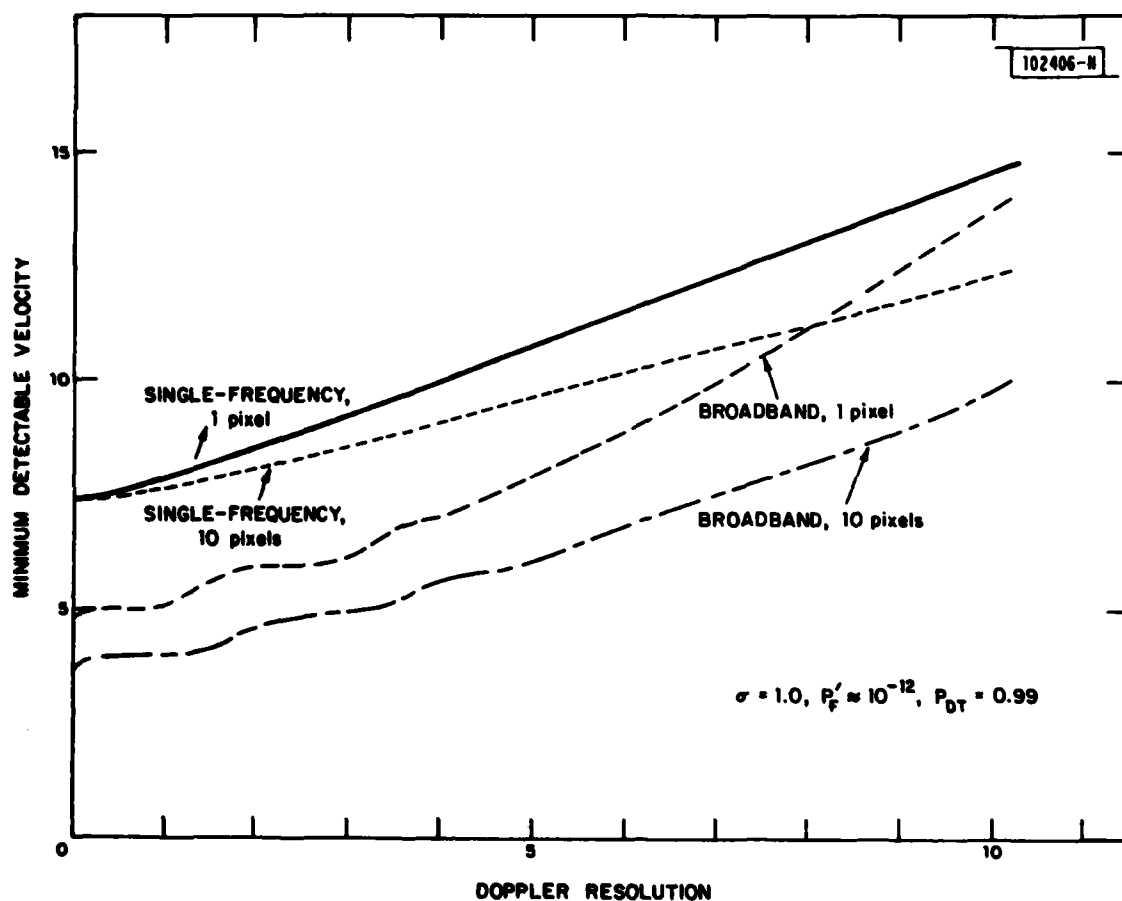
Fig. 18. Comparison of minimum detectable velocity versus Doppler resolution for $\sigma = 1$, $P_F' \approx 10^{-12}$, $P_{DT} = 0.99$ and single-pixel (- - -) and 10-pixel average (······) broadband return Gaussian statistics and single pixel (———) and 10-pixel average (- - - -) single-frequency return Gaussian statistics.

51

between the broadband and single-frequency return limits. Since
infrared radar returns are expected to have some of both types of
characters, realistic values will lie somewhere in between.

2) Pixel integration improves system performance. However, for real-
istic numbers of pixels integrated, this improvement is not very
dramatic. Consequently, pixel integration will not be a total
panacea for the minimum detectable velocity problem.

3) The minimum detectable velocity increases with increasing filter
bandwidth. Thus, the best performance is obtained with the smallest
filter bandwidth compatible with the linewidth of the target returns.
However, the smaller the bandwidth, the more filters required to
cover the entire range of expected target velocities. As a result,
the trade-off between performance and complexity must be considered.

4) For typical values ($\sigma \approx 2\omega_c \approx 1$ kmph) minimum detectable velocities
will be of the order of 5-10 kmph. Although this is not the 1-2 kmph
mentioned as a design goal in Section 1, 5-10 kmph is acceptable.

All of the preceding results have assumed a Gaussian clutter spectrum.
However, a Gaussian distribution has tails extending to infinity while real
clutter sources cannot have components with infinite velocities. In addition,
the experimental results quoted were obtained under conditions where large
numbers of independent scatters are contained within the beamwidth. Under
such conditions the law of large numbers applies and the measured distribution

52

will tend to a Gaussian regardless of the shape of the actual distribution.
As a result, the clutter spectrum may not and in fact cannot be truly
Gaussian. Therefore, Figs. 14-18 should be interpreted as giving qualitative
trends as opposed to quantitative results. For example, a sharp cutoff of
the high-velocity components would tend to reduce the minimum detectable
velocity. It is also possible that the clutter distribution may be Gaussian
out to several standard deviations. If this is true, and if the center
frequency of the filter lies within the Gaussian regime, then Figs. 14-18
will be quantitative. Experimental investigations of the clutter spectrum
at infrared frequencies are needed before the effects of clutter on MTI
performance can be conclusively evaluated.

5. ARCHITECTURE OF THE MTI ELECTRONICS

The basic components of any airborne laser Doppler MTI system are indi-
cated schematically in Fig. 19. A laser beam of known frequency content is
transmitted to the ground and the radiation reflected from the target is col-
lected and detected by a detector (or possibly an array of detectors). The
electrical signal from each detector is then frequency analyzed and the tar-
get return frequency data are processed along with data concerning the aircraft
velocity to determine the presence or absence of objects moving with respect
to the ground. Finally, the MTI signals are provided to a display or to an
automatic cuing system.

The MTI processing electronics must be capable of performing several
operations. As shown in the preceding sections both postdetection integration
and multiple pixel integration are required for maximum signal-to-noise

53
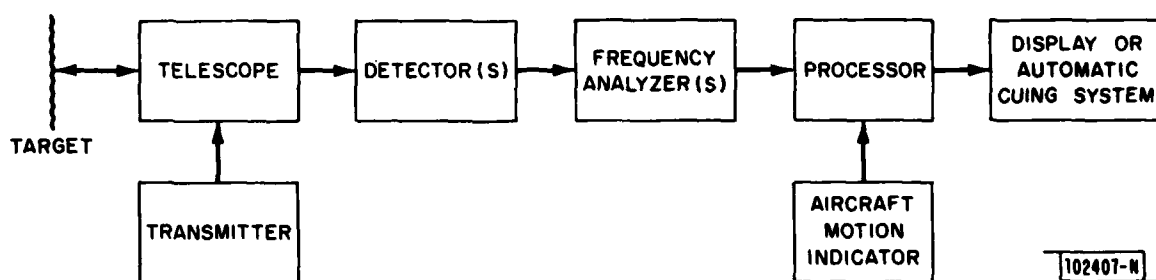
Fig. 19. Schematic diagram of an airborne laser Doppler MTI system.

54

performance. In addition, if the aircraft lacks an adequate inertial platform, the MTI processor may be required to generate its own aircraft velocity signal. Finally, the processor must incorporate some means of using the target velocity data to indicate moving targets to the pilot.

This last function can be accomplished in two basically different ways. In the first, the strongest velocity component coming from each pixel-integrated region of the field-of-view is determined and used to produce a color-coded image (different velocities would be coded in different colors in much the same manner as is done in range/intensity color mapping[13]) which is rolled down a display as the aircraft flies along. The pilot would examine this display and manually switch into the imager mode to investigate suspected targets. In an alternate approach the pixel-integrated, frequency-analyzed data would be notch-filtered (to eliminate clutter returns) and threshold detected. Any signal exceeding the threshold would cause the infrared radar to automatically switch into the imaging mode and start generating images of the region immediately surrounding the pixels which exceeded the threshold. Since the pilot will in general be too busy flying the airplane to continually scan an MTI display, we will opt for the latter approach because of its automatic cuing character.

Let us now consider the problem of determining the aircraft velocity. One of the simplest approaches is found in TACCAR (short for time-averaged-clutter coherent airborne radar) systems.[12] A schematic diagram of a

55

TACCAR-like velocity correction system is shown in Fig. 20. The heterodyne signal from a detector passes through a mixer and a portion of the mixer output feeds a frequency discriminator. The discriminator's output controls a frequency synthesizer which provides the second input to the mixer. This servo loop attempts to maintain the mixer output frequency at a constant value ω_0. However, the temporal response of the servo loop is purposefully made slower than the characteristic time scales over which the input frequency can change (i.e., the dwell time) but fast compared to the time scales over which the aircraft velocity can significantly change. Thus, the servo system will track out changes in signal frequency due to aircraft (and scanner) motions but will not respond to rapid frequency changes associated with the appearance of a moving target in the laser beam. In these systems the output of the mixer is typically passed through a band-reject filter which eliminates frequencies close to ω_0. Signals from stationary objects (which will occur at ω_0) will be rejected while the signals from moving targets (occurring at frequencies $\omega \neq \omega_0$) will be passed. The moving target signals are then detected, integrated to reduce noise (the total passband of the band-reject filter must be large compared to the dwell bandwidth in order to allow all non-zero velocities of interest to be detected), and compared against a threshold. Signals exceeding the threshold are identified as moving targets and sent to the display or automatic cuing system.
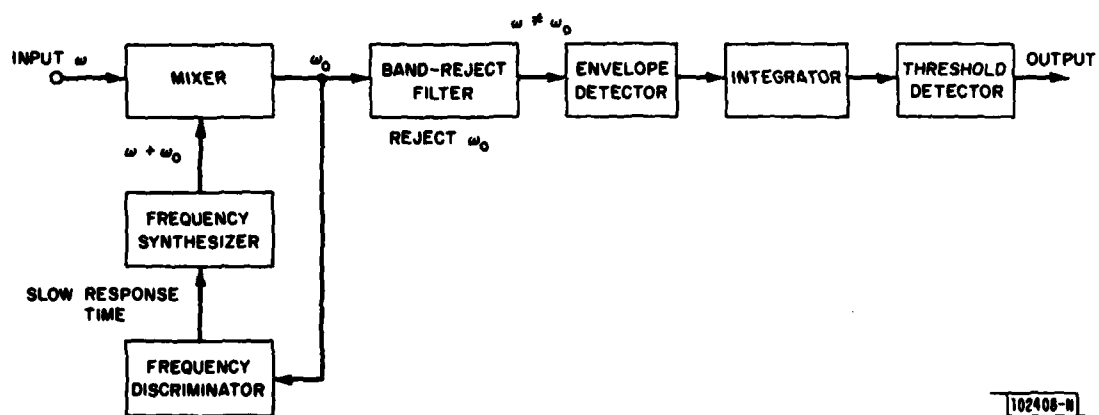
Fig. 20. Schematic diagram of a TACCAR-like MTI system using a servo loop to compensate for aircraft and scanner motions.

The TACCAR approach is not applicable to the IRAR MTI problem for two reasons both of which are traceable to the low signal-to-noise ratios encountered in the close air support scenario. First, TACCAR frequency discriminators operate by splitting an input signal into two parts and delaying one part with respect to the other. The two signals are then combined in a mixer which produces a dc voltage proportional to the relative phase between the two signals (and thus to the frequency if a nondispersive fixed delay is used). The phase of a signal can only be well-defined if the signal-to-noise ratio is high. At the signal-to-noise ratios encountered in the IRAR problem, frequency discriminators do not perform satisfactorily. Second, band-reject filter-integrator-threshold detector systems do not perform well at low signal-to-noise ratios. Consider the idealized band-reject filter in Fig. 21 with a rejection band of width $2W_1$ centered about ω_0 and passbands of width W_2 on either side of the rejected band followed by an integrator with integration time T. If $W_2 \gg W_1$ and we consider ideal (i.e., square) filter and integrator responses, the signal-to-noise ratio of the system is given by[10]

$$ \text{SNR} \approx \frac{\eta P_R T}{2\,h\,\nu} \left(1 + \left(\frac{\eta P_R}{h \nu W_2} \right)^{-1} \right)^{-1} \tag{44} $$

where η is the quantum efficiency, P_R is the incident power, and $h\nu$ is the photon energy. Noting that the heterodyne detection signal-to-noise ratio of a system with bandwidth 1/T is

$$ \text{SNR}_{hT} = \eta P_R T / h\nu \tag{45} $$

58
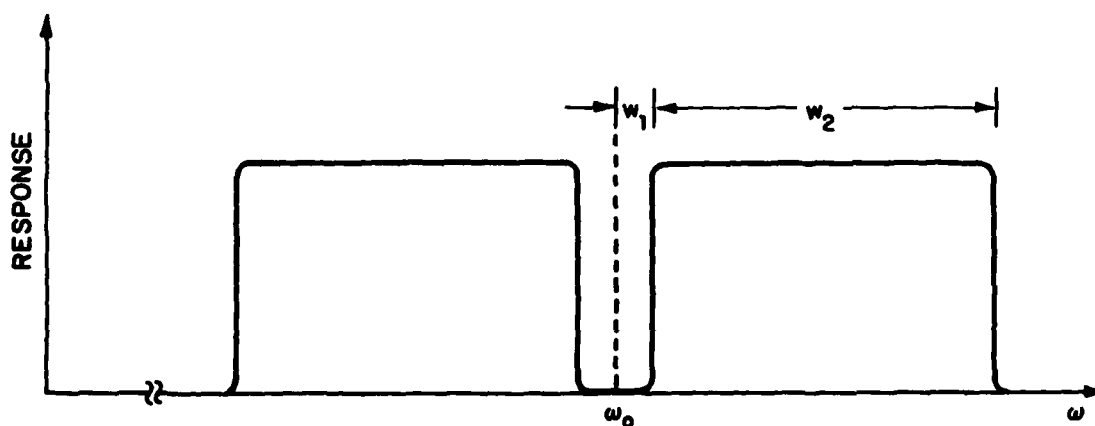
Fig. 21. Frequency response of an idealized band-reject filter. The center frequency is ω_o, the rejection band has width $2W_1$ and the passbands have width W_2.

Eq. (44) may be rewritten as

$$\text{SNR} \approx \frac{(\text{SNR}_{hT})^2}{2W_2T} \left(1 + \frac{\text{SNR}_{hT}}{W_2T}\right)^{-1} \tag{46}$$

If $\text{SNR}_{hT}/W_2T \gg 1$, Eq. (46) reduces to

$$\text{SNR} \approx \text{SNR}_{hT}/2 \tag{47}$$

while if $\text{SNR}_{hT}/W_2T \ll 1$, we find

$$\text{SNR} \approx \frac{(\text{SNR}_{hT})^2}{2W_2T} \ll \frac{\text{SNR}_{hT}}{2} \tag{48}$$

Since typical values of W_2T are in the range 100-1000 and typical values of SNR_{hT} will be less than 100, Eq. (48) indicates that the effective signal-to-noise ratio will be much reduced from its theoretical maximum. Thus, TACCAR-like systems are not desirable.

An MTI processor which does not suffer these drawbacks and incorporates all of the necessary functions is shown in Fig. 22. The output from each of N_D detectors is frequency analyzed into a number (N_C) of Doppler channels. Several potential methods of performing the frequency analysis are discussed in Section 6. Each Doppler channel is individually envelope detected and integrated. The integration time is chosen to correspond to several dwell times (e.g., ~500 μsec if $t_D \approx 100$ μsec). This accomplishes both the post-detection integration and one dimension of the pixel integration. Next all

60

Fig. 22. Schematic diagram of the proposed IRAR MTI processing electronics.

of the integrated outputs are now processed by a multiple pixel integrator. This unit groups the Doppler channels according to frequency (refer to Fig. 23) and for each frequency it sums the signals from various groups of detectors. This second dimension of pixel integration results in $M(< N_D)$ target elevation channels.
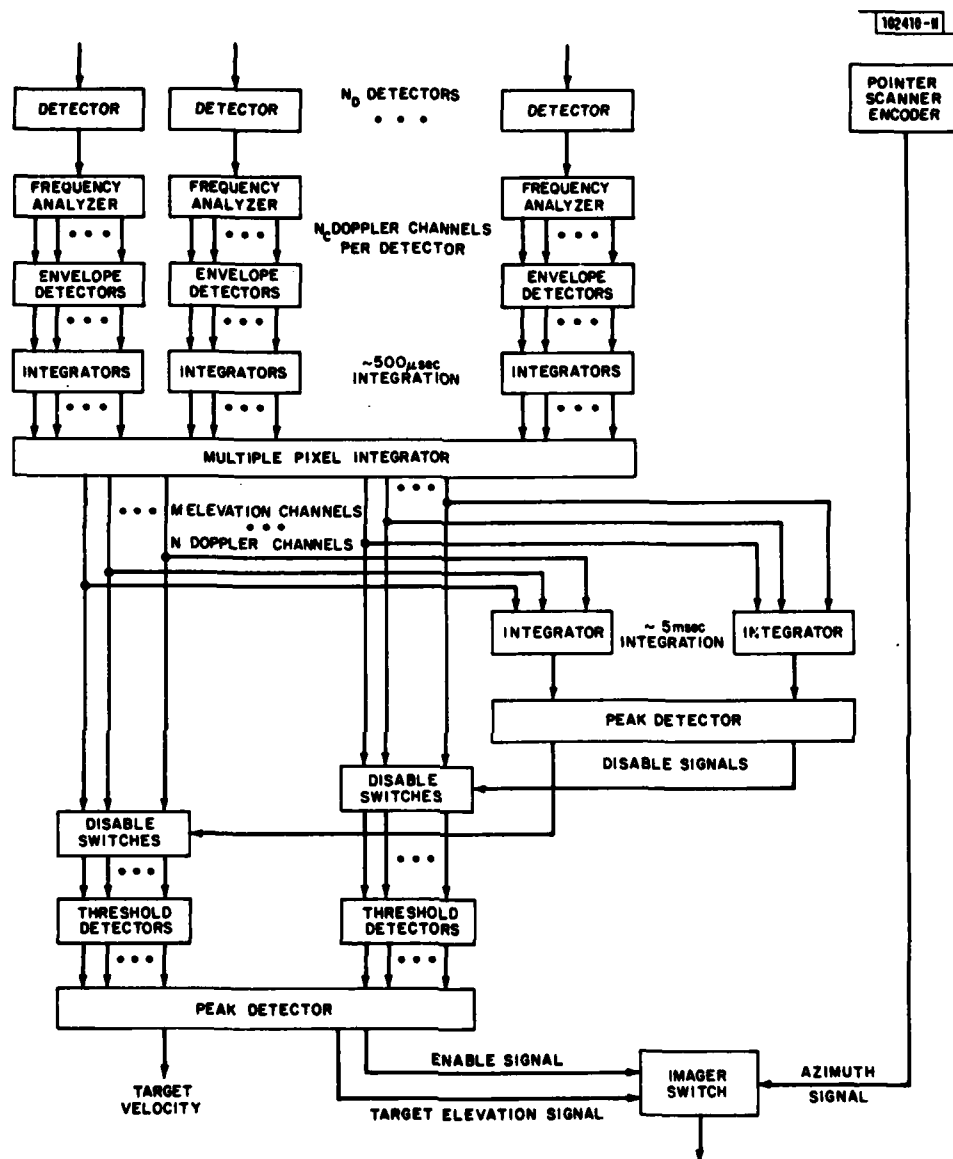
Each of the outputs from the multiple-pixel integrator is split into two parts. In one branch the outputs from the elevation channels of each frequency are summed and temporally integrated with integration times being many times the dwell time (e.g., ~ 5 msec). The integrated outputs (one for each Doppler channel) are sent to a peak detector which determines which channel has the maximum signal. A disable signal is sent to the disable switches in the corresponding Doppler channel in the second branch. The characteristic response time of the signal at the input to the peak detector in the first branch is much slower than the response time of the signal at the output of the multiple pixel integrator. Thus, although the disable circuit will compensate for slow temporal variations in the signal (such as those caused by scanner motion and aircraft velocity changes), it will not compensate for fast variations (such as those caused by the sudden appearance of a small moving target). It should be noted that because of clutter effects, disable signals may also have to be sent to switches in several Doppler channels on either side of the maximum to reduce false alarms. This, of course, determines the minimum detectable velocity.

Next, signals passed by the disable switches (and thus which correspond to non-zero velocities) are threshold detected. The threshold detector signals are sent to a peak detector which determines if a moving target is present, which elevation channel has the maximum signal, and what is the target

INPUT (N_D Detectors, N_c Doppler Channels Per Detector)
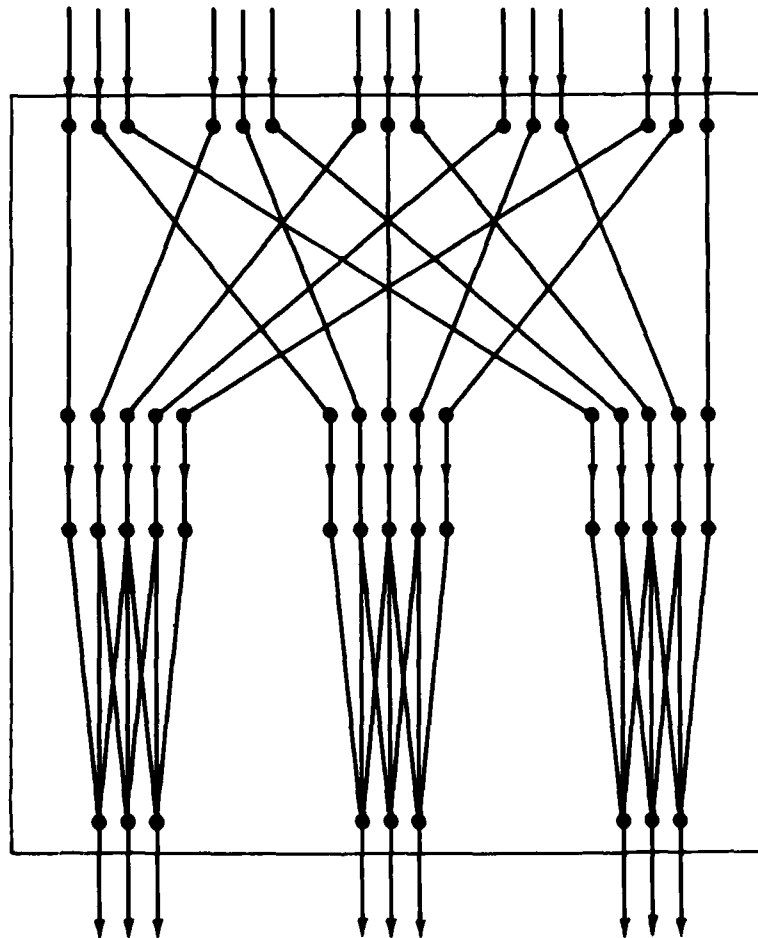
OUTPUTS (M Elevation Channels, N_c Doppler Channels Per Elevation Channel)

Fig. 23. Flow diagram of the multiple pixel integrator. The upper portion of the device performs a sorting of the outputs according to frequency while the lower portion sums (for any single frequency) the outputs from different groups of detectors. For simplicity only 5 detectors and 3 Doppler channels per detector are depicted. A similar diagram could be drawn for any desired system.

63

velocity. An enable signal from the peak detector activates a switch which converts the infrared radar from the MTI mode to the imager mode. The elevation signal is coupled with an azimuth signal from an encoder on the pointer-scanner mirror to direct the system to point the imager in the proper direction.

The MTI processor of Fig. 22 is clearly not unique and other candidate systems can be readily devised. The final design will depend in part on the technology available. For example, the system described above is quite complicated (as are other candidate systems) and has the potential for becoming quite large. However, many of the necessary operations can be performed either in a digital or discrete analog fashion. It is envisioned that charge-coupled device, microprocessor, and very large-scale integration (VLSI) technologies may be potentially useful in reducing the size of the processing electronics. The nature (e.g., serial or parallel outputs and inputs) of the devices employed will clearly affect the details of the design. Nevertheless, any proposed system must incorporate most of the features of Fig. 22.

6. FREQUENCY ANALYSIS TECHNIQUES

There are three major candidate techniques for performing the frequency analysis function: bandpass filter banks, acoustooptic deflection, and chirp z transform Fourier analysis. The first technique involves nothing more than dividing the amplified signal from the heterodyne detector into $m + 1$ parts and passing each through a different bandpass filter (Fig. 24). The filters

64

102412-N

FILTER
ω_0, $\Delta\omega$ → ENVELOPE DETECTOR →

FILTER
$\omega_0 + \Delta\omega$, $\Delta\omega$ → ENVELOPE DETECTOR →

FILTER
$\omega_0 + 2\Delta\omega$, $\Delta\omega$ → ENVELOPE DETECTOR →

INPUT SIGNAL → AMPLIFIER → 1 : m + 1 POWER DIVIDER

FREQUENCY COMPONENT OUTPUTS TO DOPPLER PROCESSOR

m-3 ADDITIONAL
FILTERS AND CRYSTAL DETECTORS

FILTER
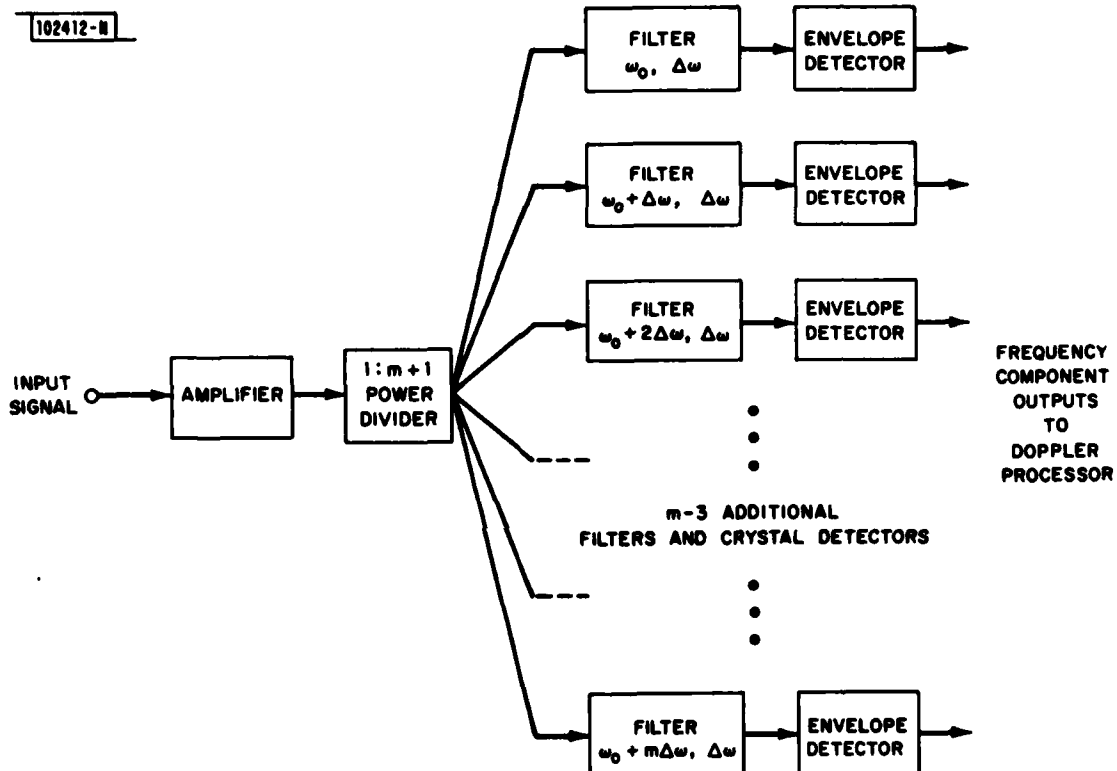$\omega_0 + m\Delta\omega$, $\Delta\omega$ → ENVELOPE DETECTOR →

Fig. 24.   Schematic diagram of a frequency analyzer employing a filter band.

65

are chosen to form a picket fence with partially overlapping passbands. Placing the overlap at the -3 dB response points of the filter gives a good compromise between channel ambiguity (having a monochromatic signal produce outputs from several filters simultaneously) and signal miss probability (not detecting a weak monochromatic signal which falls midway between the center frequencies of two adjacent filters). The picket fence response of an $m + 1$ filter bank with -3dB overlap is shown in Fig. 25. The output from each filter is then envelope detected and supplied to the Doppler processor. The net result of using the filter bank is to generate a discrete Fourier transform of the heterodyne detector output. The filter bank of Figs. 24 and 25 would produce $m + 1$ frequency components with resolution $\Delta\omega$ covering an input frequency range from $\omega_o - 1/2\ \Delta\omega$ to $\omega_o + (m + 1/2)\ \Delta\omega$. In an MTI system, $\Delta\omega$ is determined by the required velocity resolution and the input bandwidth (and hence the number of channels required)

$$B_I = (m + 1)\ \Delta\omega \tag{49}$$

is determined by range of Doppler frequencies which may be encountered. Frequency analysis using bandpass filter banks has been a proven technique for many years. However, the microwave components are rather bulky (a 100 channel filter bank might occupy $3000 - 5000\ cm^3$ and weigh $5 - 10$ kg) and therefore, this technique may not be practical for an airborne multichannel, multidetector Doppler analyzer. Acoustooptic and chirp z transform devices, on the other hand, offer significant potential savings in size and weight when high resolution, wide bandwidth devices are required.
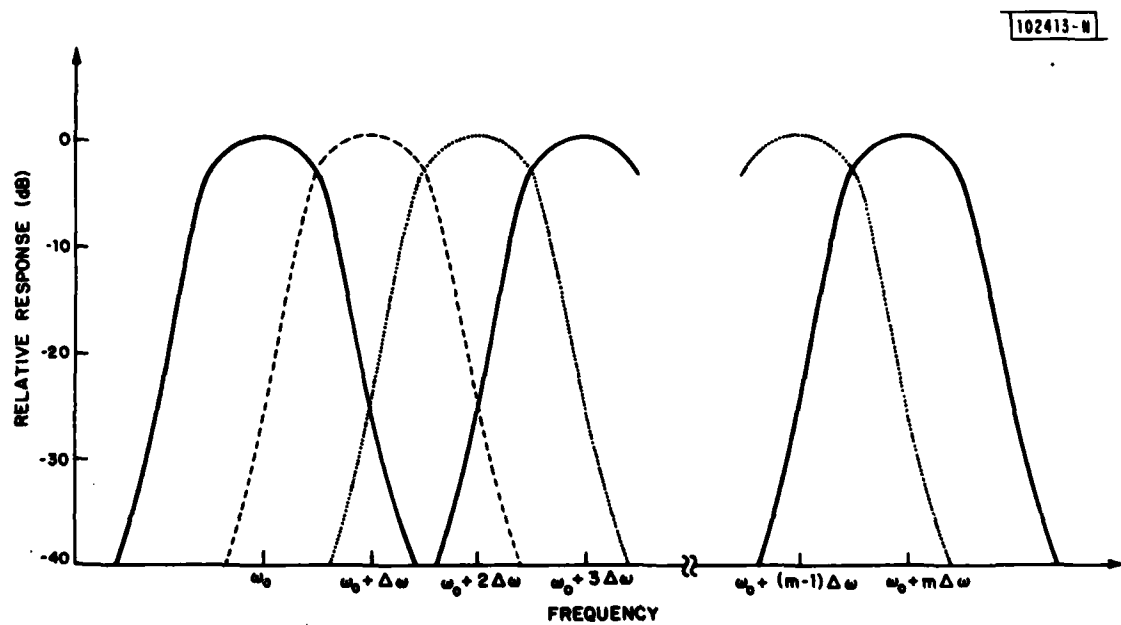
Fig. 25. Picket fence response of a filter bank of m + 1 filters which overlap at the -3 dB response points.

Acoustooptic frequency analyzers work on the principle that the angular deflection that an optical beam suffers when it interacts with an acoustic wave is a function of the frequency of the acoustic wave. As indicated in Fig. 26, in an acoustooptic frequency analyzer the signal from the heterodyne detector is amplified and transformed into an acoustic wave in a crystal (such as $LiNbO_3$) by a transducer. A fraction of the intensity of a visible laser beam incident on the crystal is deflected through various angles related to the frequency components of the acoustic wave and focused onto a detector array. Since the intensity of the laser radiation deflected through any given angle is proportional to the amplitude of the corresponding acoustic frequency component, the magnitudes of the detector outputs constitute a discrete Fourier transform of the heterodyne detector signal. Fig. 26 illustrates this behavior for an input signal containing two discrete frequencies f_1 and f_2.

The theory of acoustooptic frequency analysis has been thoroughly reviewed in the literature.[14,15] However, for completeness we will summarize the key results. Consider an acoustic grating of wavelength Λ formed in a crystal by an acoustic wave of frequency f with

$$\Lambda = V/f \qquad (50)$$

where V is the sound velocity. A light beam of free space wavelength λ_0 incident upon this grating at the Bragg angle θ_B' given by
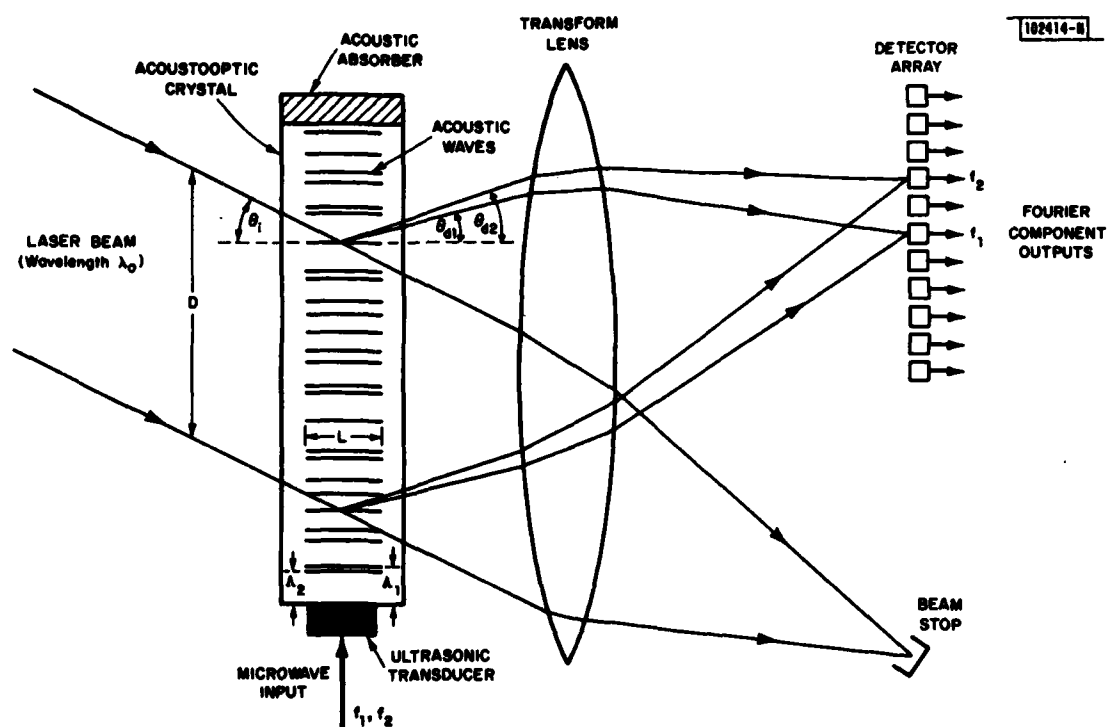
$$\sin \theta_B' = K/2k \qquad (51)$$

68

Fig. 26. Schematic diagram of an acoustooptic frequency analyzer. The acoustic wave patterns correspond to an input containing two frequencies f_1 and f_2.

where $K = 2\pi/\Lambda$, $k = 2\pi n/\lambda_o$, and n is the refractive index, will be diffracted. Conservation of momentum (Fig. 27a) requires the diffracted beam angle θ_d to equal the Bragg angle (i.e., the angle of incidence θ_i')

$$\theta_d' = \theta_B' = \theta_i'$$

In this treatment, primed angles are measured in the crystal while unprimed angles are measured external to the crystal. The two sets of angles are related by Snell's law

$$n \sin \theta' = \sin \theta \tag{52}$$

If for a fixed angle of incidence θ_i', the acoustic wavelength is close but not equal to the wavelength at which the Bragg condition is satisfied, a diffracted beam will still result even though momentum cannot be strictly conserved. The diffracted beam will occur at the angle θ_d' which minimizes the momentum mismatch. Analysis of Fig. 27b yields

$$\tan \theta_d' = (K - k \sin \theta_i') / k \cos \theta_i' \tag{53}$$

The momentum mismatch, of course, will result in a reduced diffracted intensity. The diffracted intensity normalized to the incident intensity may be expressed as

$$I_d/I_o \approx [\sin^2 \eta^{1/2}] \; [\mathrm{sinc}^2(\frac{L}{2L_o} (F^2 - F))] \tag{54}$$

$$\approx \eta \; \mathrm{sinc}^2 \; [\frac{L}{2L_o} (F^2 - F)] \tag{55}$$

70
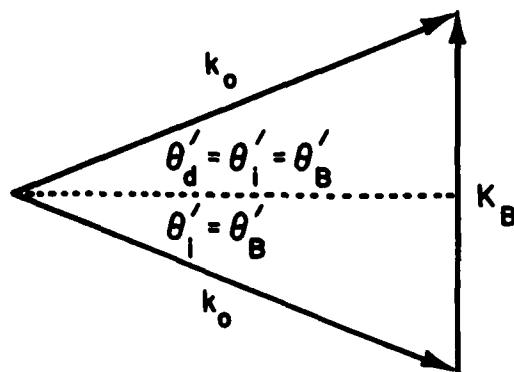
Fig. 27. Momentum conservation in the acoustooptic interaction. (a) the Bragg condition and (b) momentum mismatch at non-optimum angles of incidence.

where $F = f/f_o$ is the acoustic frequency normalized to the frequency at which Bragg matching occurs, L is the width of the acoustic beam,

$$L_o = n\Lambda_o^2 \cos \theta_i' / \lambda_o \qquad (56)$$

and $\Lambda_o = V/f_o$. The diffraction efficiency η is given by

$$\eta = \frac{\pi^2}{2\lambda_o^2} \left(\frac{n^6 p^2}{\rho V^3} \right) \frac{P_a L}{H \cos^2 \theta_i'} \qquad (57)$$

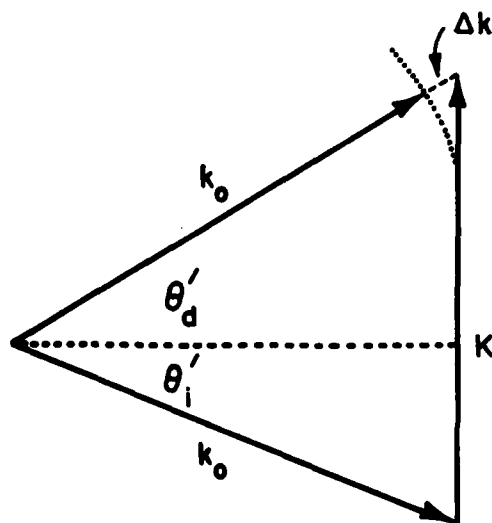where p is the crystal elastooptic coefficient, ρ is the material density, and P_a is the acoustic power in a beam of cross sectional area $L \cdot H$. From Eq. (55) the 3 dB bandwidth of the acoustooptic frequency analyzer is found to be

$$\Delta f_{3\,dB} \approx 1.8 \ f_o L_o / L \qquad (58)$$

The frequency resolution δf of an acoustooptic frequency analyzer is related to the number of acoustic wavelengths N encompassed by the laser beam. If D is the projected width of the laser beam, the resolving power is given by

$$R = \lambda/\delta\lambda = f/\delta f = N = D/\Lambda = Df/V \qquad (59)$$

Thus

$$\delta f = V/D = 1/\tau \qquad (60)$$

where τ is the acoustic transit time across the laser beam. The total number of resolvable frequency elements N contained in the bandwidth of the device is given by the time-bandwidth product

$$N = \Delta f_{3\,dB} / \delta f = \Delta f_{3\,dB}\, \tau \qquad (61)$$

Both bulk-wave and surface-wave acousto-optic frequency analyzers have been fabricated with time-bandwidth products in excess of 1000.[14-16] The latter, using integrated optics (guided optical waves, surface acoustic processing), offers potential for significant miniaturization. Unfortunately, the integrated optical devices probably cannot achieve the desired frequency resolution. This results because typical acoustic velocities are of the order of a few times 10^5 cm/sec implying laser beam widths of the order of a few cm to achieve 100 kHz resolution. Bulk wave devices can be made this large but at the present time integrated optical structures cannot.

Chirp z transform devices work on the following mathematical principles.[17] Consider an input signal $S_i(t)e^{i2\pi ft}$ passing through a chirp transversal filter with impulse response $h(t) = e^{i2\pi f_0 t}\, e^{i\alpha t^2}$. Suppressing the carrier frequency dependence, the output of the transversal filter is given by the convolution of S_i with h

$$S_o(\tau) = \int_{-\infty}^{\infty} S_i(t)\, e^{i\alpha(t-\tau)^2}\, dt \qquad (62)$$

Expanding the exponent yields

$$S_0(\tau) = e^{i\alpha\tau^2} \int_{-\infty}^{\infty} S_i(t) e^{i\alpha t^2} e^{-i2\alpha\tau t} \, dt \tag{63}$$

which except for the $e^{i\alpha\tau^2}$ weighting factor is the Fourier transform (with transform variable $\omega = 2\alpha\tau$) of the function $S_i(t) e^{i\alpha t^2}$. If we define a signal $S'(t)$, premultiplied by a chirp $e^{-i\alpha t^2}$ such that

$$S_i(t) = S'_i(t) \, e^{-i\alpha t^2} \tag{64}$$

and an output signal which is the transversal filter output multiplied by a chirp

$$S'_0(\tau) = S_0(\tau) \, e^{-i2\alpha\tau^2} \tag{65}$$

we find

$$S'_0(\tau) = \int_{-\infty}^{\infty} S'_i(t) \, e^{-2\alpha\tau t} \, dt \tag{66}$$

That is, $S'_0(\tau)$ is the Fourier transform of $S'_i(t)$. If the chirps are of finite duration and repetitive, a finite Fourier transform operation is performed.

The chirp z Fourier transformation can be implemented by a system shown schematically in Fig. 28.[17] Impulse inputs to two chirp transversal filters generate the chirps $e^{-i\alpha t^2}$ and $e^{-i\alpha\tau^2}$ which multiply the input and output signals, respectively. A third chirp transversal filter performs the required convolution.
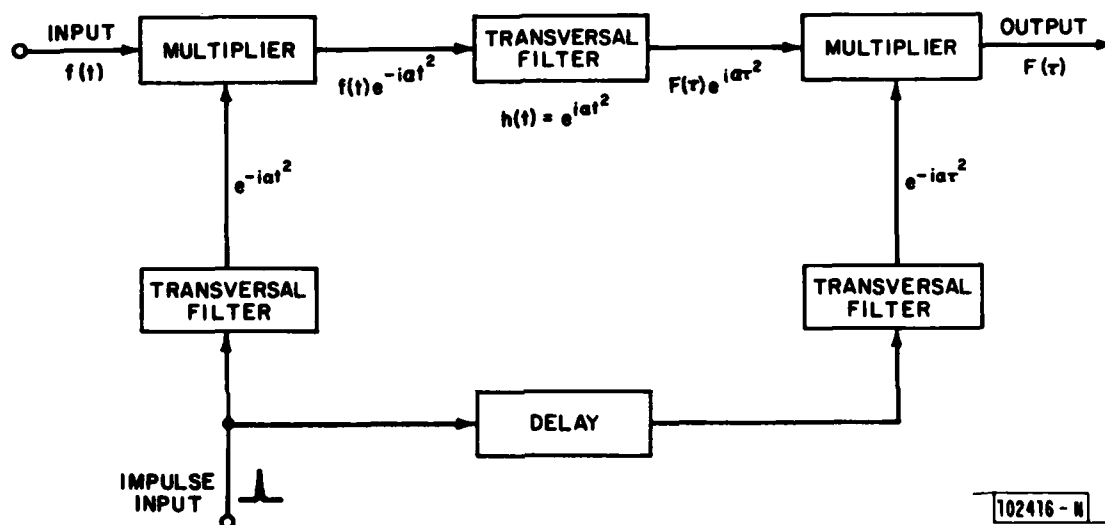
74

Fig. 28. Schematic diagram of a chirp z transformation frequency analyzer.

75

A chirp transversal filter can be considered as an ideal linear dispersive delay line. In such a delay line the delay encountered by a monochromatic wave is proportional to its frequency. Clearly, the impulse response of such a linear dispersive delay line is a linear frequency chirp. The direction (sign) and rate of the chirp is proportional to the frequency dispersion while the maximum amplitude of the chirp is given by the bandwidth of the delay line.

Surface acoustic wave (SAW) devices can be used to realize a linear dispersive delay line at microwave frequencies. Consider the reflective array compressor (RAC) shown in Fig. 29.[17] Surface acoustic waves are generated by a transducer and propagate through an array of parallel grooves etched in the surface of the crystal. The grooves are oriented at an angle θ to the direction of propagation of the incident surface acoustic waves. When the waves encounter a sequence of grooves whose spacing G is such that constructive interference can occur, the acoustic waves will be reflected at right angles. The depth of the grooves controls the reflection coefficient. The reflected waves encounter a second mirror image array, are reflected again, and propagate to an output transducer. Since the acoustic velocity is independent of frequency, the delay encountered by any acoustic frequency is proportional to the total path length travelled. Consequently, by controlling the sequence of groove spacings different delays can be obtained for different frequencies. Minor groove spacing (phase) errors can be compensated by depositing a film of varying width between the two arrays (as shown in Fig. 29).
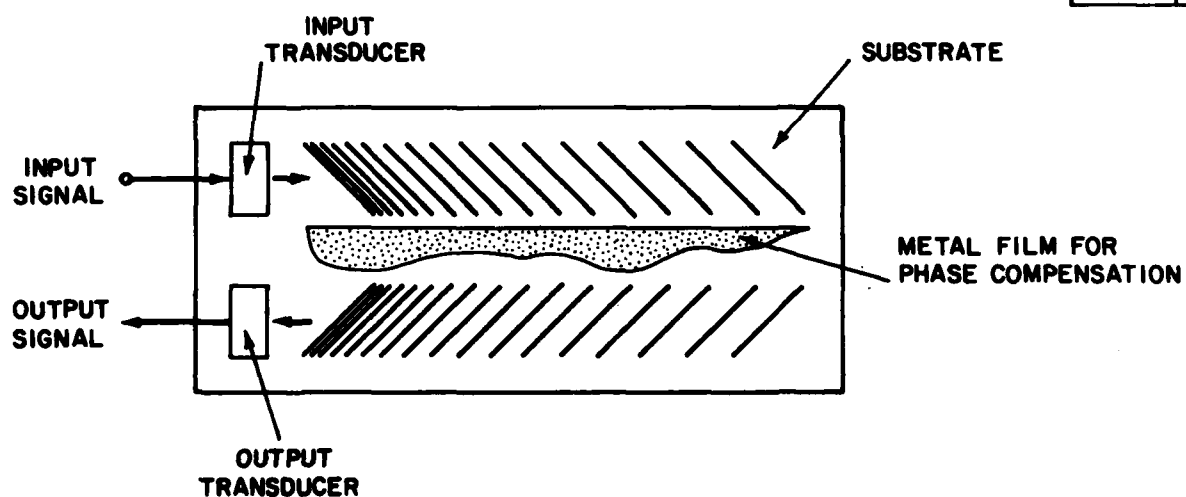
Fig. 29. Schematic diagram of a reflective array compressor (RAC) transversal filter.

In many materials, the surface wave velocities differ along the incident and transverse propagation directions. Therefore, the groove angle θ need not be 45°. Consider Fig. 30. If v_1 and v_2 represent the surface wave velocities in the incident and transverse directions, then the requirement that reflection generates a flat wavefront at right angles requires the path lengths $\overline{ABD}$ and $\overline{AC}$ to differ by a wavelength,

$$\overline{AB} + \overline{BD} = \overline{AC} + \lambda_1 \tag{67}$$

where $\lambda_{1,2} = v_{1,2}/f$. The same path length condition applied to the time reversed wavefront requires

$$\overline{DB} + \overline{BA} = \overline{DC} + \lambda_2 \tag{68}$$

Since $\overline{AB} = G/\cos\theta$, $\overline{DB} = G/\sin\theta$, $\overline{AC} = \overline{BD}$, and $\overline{DC} = \overline{BA}$, we have

$$G = \lambda_1 \cos\theta = \lambda_2 \sin\theta \tag{69}$$

from which we determine

$$\tan\theta = \lambda_1/\lambda_2 = v_1/v_2 \tag{70}$$

A linear chirp will be generated when the groove spacing is linearly proportional to the distance from the transducer. Although it will not be demonstrated here, the proper groove positions are given by

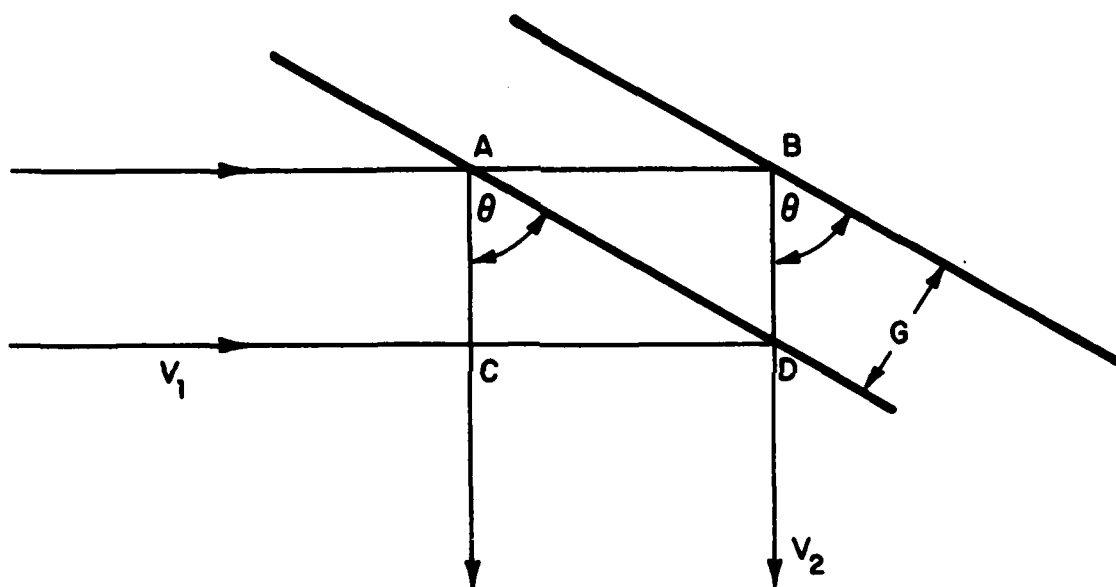$$x_n + \frac{B\lambda_o}{2V_1^2 T} x_n^2 = \frac{n\lambda_o}{2} \tag{71}$$

Fig. 30. Relationship between groove angle and acoustic wave velocities in a reflective array compressor.

where x_n is the position of the nth groove. The impulse response of this filter is

$$h(t) = e^{i2\pi f_o t(1 + Bt/2f_o T)} \qquad -\frac{T}{2} < t < \frac{T}{2} \qquad (72)$$

where $f_o = V_1/\lambda_o$ and the instantaneous frequency f is

$$f = f_o + \frac{Bt}{T} \qquad (73)$$

and varies linearly from $f_o - B/2$ to $f_o + B/2$.

Both the acoustooptic and the chirp z transform techniques are potentially capable of accomplishing the frequency analysis required by the IRAR MTI subsystem in packages of reasonable size. However, both technologies are still developing and devices capable of meeting our specifications while operating in an aircraft environment have not yet been demonstrated. Further work on these devices is clearly required before they can be incorporated into an airborne system.

7. CONCLUSIONS

The work presented in this report appertains to a very specific system. Therefore, minor changes in initial design parameters can have a significant impact on the numerical conclusions arrived at here. However, certain general conclusions can be drawn which pertain to airborne infrared radar MTI systems as a whole.

First, weather penetration effects, compactness, efficiency, high power, and high frequency stability favor using a cw CO_2 laser transmitter and hetero-

dyne detection in a Doppler MTI system.

Second, the ability to completely cover a wide field-of-view in a target acquisition mode will probably require the use of large detector arrays. In a line scan search mode the optimum signal-to-noise ratio is achieved by a linear detector array with just enough detectors to adequately cover the field-of-view.

Third, pixel integration will be required in many situations to produce desired detection and false alarm probabilities. In any situation pixel integration will improve the weather penetration capability of a system.

Fourth, ground clutter will probably limit obtainable minimum detectable target velocities to values of the order of 5 kmph or larger even though the velocity resolution may be of the order of 1 kmph.

Fifth, the size of the MTI electronics can impose a serious constraint on system utility. However, careful architecture of the processing electronics as well as judicious use of developing acoustooptic, charge-coupled device, very large-scale integration, and surface acoustic wave technologies may ameliorate this situation.

Lastly, an MTI system can share most of the components of an imaging infrared radar system. This should enable multifunction infrared radar systems to be built using a single optical train.

REFERENCES

1. R. J. Becherer, "System Design Study for Infrared Airborne Radar (IRAR)," Technical Note 1977-29, Lincoln Laboratory, M.I.T. (18 October 1977), DDC AD-A048979/9.

2. R. C. Harney, "Conceptual Design of a Multifunction Infrared Radar for the Tactical Aircraft Ground Attack Scenario," Project Report TST-25, Lincoln Laboratory, M.I.T. (25 August 1978), DDC AD-A061048/5.

3. R. J. Hull and S. Marcus, Proc. 1978 National Aerospace and Electronics Conf. (IEEE, Dayton, Ohio, 16 - 18 May 1978) p.662.

4. A. P. Modica and H. Kleiman, "Statistics of Global IR Atmospheric Transmission," Project Report TT-7, Lincoln Laboratory, M.I.T. (3 March 1976), DDC AD-A024311/3.

5. S. Marcus and J. W. Caunt, "A Compact CO_2 Laser for Infrared Heterodyne Radar," Rev. Sci. Instr. 49, 1410 (1978).

6. S. P. Tomczak, "Diffuse Target Scintillation in 10.6 µm Laser Radar," Project Report TT-9, Lincoln Laboratory, M.I.T. (8 March 1976), DDC-AD-A024310/5.

7. M. I. Skolnik, Introduction to Radar Systems (McGraw-Hill, New York, 1962).

8. J. H. Shapiro, "Imaging and Target Detection with a Heterodyne-Reception Optical Radar," Project Report TST-24, Lincoln Laboratory, M.I.T. (13 October 1978), DDC AD-A063767.

9. H. L. Van Trees, Detection, Estimation, and Modulation Theory, Part I (Wiley, New York, 1968), Chapters 2 and 4.

10. J. H. Shapiro, unpublished work.

11. J. V. DiFranco and W. L. Rubin, Radar Detection (Prentice-Hall, Englewood Cliffs, NJ, 1968), Chapters 2 and 4.

12. W. W. Shrader, "MTI Radar," Chapter 17 in Radar Handbook, M. I. Skolnik, Ed. (McGraw-Hill, New York, 1970).

13. R. C. Harney, J. S. Martin, and D. R. Sullivan, "Quasi-Three-Dimensional Display of Infrared Radar Images Using Rage/Intensity Color Mapping," Technical Note 1978-44, Lincoln Laboratory, M.I.T. (6 December 1978), DDC AD-A070671.

14. I. C. Chang, "Acoustooptic Devices and Applications," IEEE Trans. Sonics and Ultrasonics SU-23, 2 (1976).

15. D. L. Hecht, "Spectrum Analysis Using Acousto-Optic Devices," Proc. SPIE Vol. 90: Acousto-Optics (Society of Photo-Optical Instrumentation Engineers, San Diego, California, 1976), p. 148.

16. C. S. Tsai, L. T. Nguyen, B. Kim and I. W. Yao, "Guided-Wave Acousto-Optic Signal Processors for Wideband Radar Systems," Proc. SPIE Vol. 128: Effective Utilization of Optics in Radar Systems (Society of Photo-Optical Instrumentation Engineers, Huntsville, Alabama, 1977), p. 68.

17. E. A. Ash, "Fundamentals of Signal Processing Devices," Chapter 4 in Acoustic Surface Waves, A. A. Oliner, Ed. (Springer-Verlag, Berlin, 1978).

SECURITY CLASSIFICATION OF THIS PAGE (When Data Entered)

REPORT DOCUMENTATION PAGE	READ INSTRUCTIONS BEFORE COMPLETING FORM

1. REPORT NUMBER	2. GOVT ACCESSION NO.	3. RECIPIENT'S CATALOG NUMBER
ESD-TR-80-83	AD-A091 927	

4. TITLE (and Subtitle)

Design Considerations for the Infrared Airborne Radar (IRAR) MTI Subsystem

5. TYPE OF REPORT & PERIOD COVERED

Project Report

6. PERFORMING ORG. REPORT NUMBER

Project Report TST-26

7. AUTHOR(s)

Robert C. Harney

8. CONTRACT OR GRANT NUMBER(s)

F19628-80-C-0002

9. PERFORMING ORGANIZATION NAME AND ADDRESS

Lincoln Laboratory, M.I.T.
P.O. Box 73
Lexington, MA 02173

10. PROGRAM ELEMENT, PROJECT, TASK AREA & WORK UNIT NUMBERS

Program Element No. 63250F
Project No. 649L

11. CONTROLLING OFFICE NAME AND ADDRESS

Air Force Systems Command, USAF
Andrews AFB
Washington, DC 20331

12. REPORT DATE

21 July 1980

13. NUMBER OF PAGES

92

14. MONITORING AGENCY NAME & ADDRESS (if different from Controlling Office)

Electronic Systems Division
Hanscom AFB
Bedford, MA 01731

15. SECURITY CLASS. (of this report)

Unclassified

15a. DECLASSIFICATION DOWNGRADING SCHEDULE

16. DISTRIBUTION STATEMENT (of this Report)

Approved for public release; distribution unlimited.

17. DISTRIBUTION STATEMENT (of the abstract entered in Block 20, if different from Report)

18. SUPPLEMENTARY NOTES

None

19. KEY WORDS (Continue on reverse side if necessary and identify by block number)

moving target indicators	signal-to-noise ratio	detector arrays
infrared airborne radar	clutter	frequency analysis
Doppler MTI system	detection probability	
Doppler resolution	false alarm probability	

20. ABSTRACT (Continue on reverse side if necessary and identify by block number)

A design for a moving target indication (MTI) subsystem for the infrared airborne radar (IRAR) is investigated. A Doppler MTI system incorporating heterodyne detection and a cw CO_2 laser is determined to be the most suitable approach. Numerous analyses of topics including field-of-view coverage, Doppler resolution, signal-to-noise ratio, clutter effects, etc. are presented which serve to define component specifications and processing requirements. The potential architecture of the MTI system is discussed and the impact of developing technologies on system and component design is estimated.

DD FORM 1473 EDITION OF 1 NOV 65 IS OBSOLETE
1 JAN 73

SECURITY CLASSIFICATION OF THIS PAGE (When Data Entered)